

Anatomy of the binary black hole recoil: A multipolar analysis

Jeremy D. Schnittman,¹ Alessandra Buonanno,¹ James R. van Meter,^{2,3} John G. Baker,² William D. Boggs,⁴
Joan Centrella,² Bernard J. Kelly,² and Sean T. McWilliams⁴

¹Maryland Center for Fundamental Physics, Department of Physics, University of Maryland, College Park, Maryland 20742, USA

²Gravitational Astrophysics Laboratory, NASA Goddard Space Flight Center, 8800 Greenbelt Road, Greenbelt, Maryland 20771, USA

³Center for Space Science & Technology, University of Maryland Baltimore County, Physics Department,
1000 Hilltop Circle, Baltimore, Maryland 21250, USA

⁴Department of Physics, University of Maryland, College Park, Maryland 20742, USA

(Received 2 July 2007; published 19 February 2008)

We present a multipolar analysis of the gravitational recoil computed in recent numerical simulations of binary black hole coalescence, for both unequal masses and nonzero, nonprecessing spins. We show that multipole moments up to and including $\ell = 4$ are sufficient to accurately reproduce the final recoil velocity (within $\approx 2\%$) and that only a few dominant modes contribute significantly to it (within $\approx 5\%$). We describe how the relative amplitudes, and more importantly, the relative phases, of these few modes control the way in which the recoil builds up throughout the inspiral, merger, and ringdown phases. We also find that the numerical results can be reproduced by an “effective Newtonian” formula for the multipole moments obtained by replacing the radial separation in the Newtonian formulas with an effective radius computed from the numerical data. Beyond the merger, the numerical results are reproduced by a superposition of three Kerr quasinormal modes. Analytic formulas, obtained by expressing the multipole moments in terms of the fundamental quasinormal modes of a Kerr black hole, are able to explain the onset and amount of “antikick” for each of the simulations. Lastly, we apply this multipolar analysis to help explain the remarkable difference between the amplitudes of planar and nonplanar kicks for equal-mass spinning black holes.

DOI: [10.1103/PhysRevD.77.044031](https://doi.org/10.1103/PhysRevD.77.044031)

PACS numbers: 04.25.dg, 04.25.Nx, 04.30.Db, 04.70.Bw

I. INTRODUCTION

After the recent breakthrough in numerical relativity (NR) [1–3], a number of different groups are now able to evolve binary black holes (BHs) through merger [4–6]. Recently, a great deal of effort has been directed towards the computation of the recoil velocity of the final BH [7–15]. The fundamental cause of this recoil is a net linear-momentum flux in the gravitational radiation, due to some asymmetry in the system [16–20], typically unequal masses or spins in the case of BH binaries. The recoil has great astrophysical importance because it can affect the growth of supermassive black holes (SMBHs) in the early universe [21–24]. In those scenarios dark-matter haloes grow through hierarchical mergers. The SMBHs at the centers of such haloes are expected to merge unless one has been kicked out of the gravitational potential well because the recoil velocity it gained in a prior merger is larger than its halo’s escape velocity.

Other astrophysical implications include the displacement of the SMBH, along with its gaseous accretion disk, forming an “off-center” quasar [25]. These quasars might also have emission lines highly redshifted or blueshifted relative to the host galaxy due to the Doppler shift of the recoil velocity [26]. Additionally, these displaced SMBHs could in turn displace a significant amount of stellar mass from the galactic nucleus as they sink back to the center via dynamical friction, forming a depleted core of missing mass on the order of twice the SMBH mass [22,27,28].

Numerical simulations have now been used to compute recoil velocities for nonspinning unequal-mass BH binary systems [7–9] in the range $m_2/m_1 = (1, \dots, 4)$, where m_1 and m_2 are the individual BH masses; for spinning, nonprecessing binary BHs [10–12]; and also for precessing BHs with equal [13,14] as well as unequal masses [15]. Quite interestingly, there exist initial spin configurations for which the recoil velocity can be quite large, e.g., ≥ 3000 km/sec [13–15,29]. However, it is not yet clear whether those very large recoil velocities are astrophysically likely [23,30–32]. So far, due to limited computational resources, the numerical simulations have explored a rather small portion of the total parameter space.

Analytic calculations, based on the post-Newtonian (PN) expansion of Einstein’s field equations [33] and PN-resummation techniques [34–39], have made predictions for the recoil velocity [40–44] before the NR breakthrough. Since the majority of the linear-momentum flux is emitted during the merger and ringdown (RD) phases, it is difficult to make definitive predictions for the recoil using *only* analytic methods. These methods need to be somehow calibrated to the NR results, so that they can be accurately extended during the transition from inspiral to RD. So far, in the nonspinning case, the PN model [43] has provided results consistent with NR all along the adiabatic inspiral; the effective-one-body (EOB) model [34,35,37] can reproduce the total recoil, including the contribution from the RD phase, but with large uncertainties [44]. In Ref. [45], perturbative calculations that make use of the so-

called close-limit approximation [46] have been used to predict the recoil for unequal-mass binary BHs moving on circular and eccentric orbits. More recently, Ref. [47] provided the first estimates of the distribution of recoil velocities from spinning BH mergers using the EOB model, calibrated to the NR results.

In this paper we present a diagnostic of the physics of the recoil, trying to understand how it accumulates during the inspiral, merger, and RD phases. The majority of the analysis is based on several numerical simulations of non-spinning, unequal-mass binary systems, as well as spinning, nonprecessing binary systems obtained by the Goddard numerical relativity group. What we learn in this study will be used in a forthcoming paper to improve the PN analytic models [43,44,47], so that they can be used to interpolate between NR results, efficiently and accurately covering the entire parameter space.

We frame our understanding using the multipolar formalism originally laid out by Thorne [48–52]. We work out which multipole moments contribute most significantly to the recoil. We employ analytic, but leading-order, formulas for the linear-momentum flux during the inspiral phase, and express the multipole moments in terms of a linear superposition of quasinormal modes (QNMs) during the RD phase [53]. These analysis tools help us understand why for some binary mass and spin configurations the so-called “antikick” is larger than in other cases. By antikick, we mean that the recoil velocity reaches a maximum value before decreasing to a final, smaller velocity asymptotically. As shown in Ref. [12], even a relatively small range of binary parameters can give rise to a large variety of antikick magnitudes (and even the complete lack of an antikick in some cases).

An example of this multipole analysis is shown in Fig. 1, which plots the recoil velocity as a function of time (black curve), along with the separate contributions from the mass-quadrupole–mass-octupole (red), mass-quadrupole–current-quadrupole (blue), and mass-quadrupole–mass-hexadecapole (green) moments. This plot corresponds to a nonspinning system with mass ratio of 1:2. Note, in particular, how the modes add both constructively and destructively to give the total recoil. For the nonspinning, unequal-mass systems, the kick and antikick are dominated by the mass-quadrupole–mass-octupole modes, but also receive significant contributions from the other mode pairs. For all of the simulations presented in this paper, we scale the time axis around t_{peak} , the time at which the mass-quadrupole mode reaches a maximum, closely corresponding to the peak in gravitational wave power, as well as the time that a single horizon is formed and the ringdown phase begins.

This paper is organized as follow. In Sec. II, after introducing our definitions and notations, we review the binary parameters used in the numerical simulations and examine the main features of the numerical runs. In Sec. III

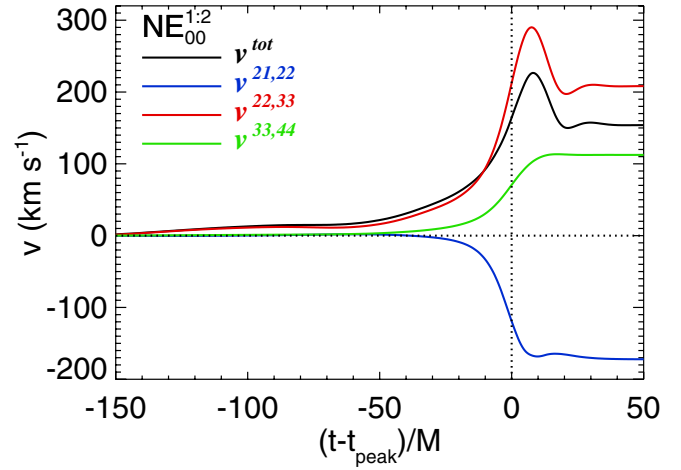


FIG. 1 (color online). The recoil velocity as a function of time for a binary BH system with mass ratio 1:2 and no spins. The total recoil is plotted in black, along with the contributions from different mode pairs, described below in Sec. III. We denote by t_{peak} the time at which the multipole l^{22} reaches its maximum (see Sec. III).

we discuss the multipolar expansion of the linear-momentum, angular-momentum, and energy fluxes given in terms of the symmetric trace-free radiative mass and current moments, and show how to compute those fluxes from the multipole decomposition of the Weyl scalar Ψ_4 . In Sec. IV, we analyze the multipole content of the numerical waveforms during the inspiral and ringdown phases. In Sec. V we show that, by properly normalizing the binary radial separation, the multipole moments computed at leading order in an expansion in $1/c$ can approximate quite well the numerical results. Moreover, a superposition of three QNMs matches the RD phase. In Sec. VI we apply the tools developed in the previous sections to understand, using analytic expressions, how the kick builds up during the inspiral, merger, and ringdown phases. We also apply these methods to help explain the large difference between planar and nonplanar kicks from equal-mass spinning BHs [10,13,15]. Finally, Sec. VII contains a brief discussion of our main results and future research directions. In the Appendix we discuss recent results for mass ratio 1:4.

II. NUMERICAL SIMULATIONS

In this section we introduce our definitions and notation, and review the main features of the numerical simulations. Throughout the paper, we adopt geometrical units with $G = c = 1$ (unless otherwise specified) and metric signature $(-1, 1, 1, 1)$.

A. Definitions and conventions

Our complex null tetrad is defined using the timelike unit vector normal to a given hypersurface \hat{r} , the radial unit

vector \hat{r} , and ingoing ($\vec{\ell}$) and outgoing (\vec{n}) null vectors as

$$\vec{\ell} \equiv \frac{1}{\sqrt{2}}(\hat{\tau} + \hat{r}), \quad (1a)$$

$$\vec{n} \equiv \frac{1}{\sqrt{2}}(\hat{\tau} - \hat{r}). \quad (1b)$$

We define the complex null vectors \vec{m} and \vec{m}^* by

$$\vec{m} \equiv \frac{1}{\sqrt{2}}(\hat{\theta} + i\hat{\phi}), \quad (2a)$$

$$\vec{m}^* \equiv \frac{1}{\sqrt{2}}(\hat{\theta} - i\hat{\phi}), \quad (2b)$$

with the standard spherical metric at infinity $ds^2 = -d\tau^2 + dr^2 + r^2(d\theta^2 + \sin^2\theta d\phi^2)$. The orthogonality relations of this tetrad are then

$$\vec{\ell} \cdot \vec{\ell} = \vec{n} \cdot \vec{n} = \vec{m} \cdot \vec{m} = \vec{m}^* \cdot \vec{m}^* = 0, \quad (3a)$$

$$\vec{\ell} \cdot \vec{n} = -\vec{m} \cdot \vec{m}^* = -1, \quad (3b)$$

$$\vec{\ell} \cdot \vec{m} = \vec{\ell} \cdot \vec{m}^* = \vec{n} \cdot \vec{m} = \vec{n} \cdot \vec{m}^* = 0. \quad (3c)$$

In terms of this tetrad, the complex Weyl scalar Ψ_4 is given by

$$\Psi_4 \equiv C_{abcd}n^a(m^b)^*n^c(m^d)^*, \quad (4)$$

where C_{abcd} is the Weyl tensor and $*$ denotes complex conjugation.

To relate Ψ_4 to the gravitational waves (GWs), we note that in the transverse-traceless (TT) gauge (see Chap. 35 in Ref. [54])

$$\begin{aligned} \frac{1}{4}(\ddot{h}_{\hat{\theta}\hat{\theta}}^{TT} - \ddot{h}_{\hat{\phi}\hat{\phi}}^{TT}) &= -R_{\hat{\tau}\hat{\theta}\hat{\tau}\hat{\theta}} = -R_{\hat{\tau}\hat{\phi}\hat{\tau}\hat{\phi}} = -R_{\hat{\tau}\hat{\theta}\hat{\tau}\hat{\phi}} \\ &= R_{\hat{\tau}\hat{\phi}\hat{\tau}\hat{\theta}} = R_{\hat{\tau}\hat{\theta}\hat{\tau}\hat{\theta}} = R_{\hat{\tau}\hat{\phi}\hat{\tau}\hat{\phi}}, \end{aligned} \quad (5a)$$

$$\frac{1}{2}\ddot{h}_{\hat{\theta}\hat{\phi}}^{TT} = -R_{\hat{\tau}\hat{\theta}\hat{\tau}\hat{\phi}} = -R_{\hat{\tau}\hat{\phi}\hat{\tau}\hat{\theta}} = R_{\hat{\tau}\hat{\theta}\hat{\tau}\hat{\theta}} = R_{\hat{\tau}\hat{\phi}\hat{\tau}\hat{\phi}}. \quad (5b)$$

Following usual convention, we take the h_+ and h_\times polarizations of the GW to be given by

$$\ddot{h}_+ = \frac{1}{2}(\ddot{h}_{\hat{\theta}\hat{\theta}}^{TT} - \ddot{h}_{\hat{\phi}\hat{\phi}}^{TT}), \quad (6a)$$

$$\ddot{h}_\times = \ddot{h}_{\hat{\theta}\hat{\phi}}^{TT}. \quad (6b)$$

Since the Riemann and Weyl tensors coincide in vacuum regions of the spacetime ($R_{abcd} = C_{abcd}$), we find by combining the above equations

$$\Psi_4 = -(\ddot{h}_+ - i\ddot{h}_\times). \quad (7)$$

Note that this expression for Ψ_4 is tetrad-dependent. Here we assume the tetrad given in Ref. [55], Eqs. (5.6). It is also common for Ψ_4 to be scaled according to an asymptotically Kinnersley tetrad [Ref. [55], Eqs. (5.9)] which introduces a factor of 2 as in Ref. [56].

It is most convenient to deal with Ψ_4 in terms of its harmonic decomposition. Given the definition of Ψ_4 in Eq. (4) and the fact that \vec{m}^* carries a spin weight of -1 ,

it is appropriate to decompose Ψ_4 in terms of spin-weight -2 spherical harmonics $-2Y_{\ell m}(\theta, \varphi)$ [57]. There is some freedom in the definition of the spin-weighted spherical harmonics. Here, we define them as a linear combination of the scalar spherical harmonics $Y_{\ell m}$ and $Y_{(\ell-1)m}$, as in Ref. [58]:

$$\begin{aligned} {}_{\pm 2}Y_{\ell m}(\theta, \varphi) &= \left[\frac{(\ell-2)!}{(\ell+2)!} \right]^{1/2} [\alpha_{(\ell m)}^{\pm}(\theta)Y_{\ell m}(\theta, \varphi) \\ &\quad + \beta_{(\ell m)}^{\pm}(\theta)Y_{(\ell-1)m}(\theta, \varphi)], \end{aligned} \quad (8)$$

for $\ell \geq 2$ and $|m| \leq \ell$, and with the functional coefficients

$$\alpha_{(\ell m)}^{\pm}(\theta) = \frac{2m^2 - \ell(\ell+1)}{\sin^2\theta} \mp 2m(\ell-1)\frac{\cot\theta}{\sin\theta} + \ell(\ell-1)\cot^2\theta, \quad (9a)$$

$$\beta_{(\ell m)}^{\pm}(\theta) = 2 \left[\frac{2\ell+1}{2\ell-1}(\ell^2 - m^2) \right]^{1/2} \left(\pm \frac{m}{\sin^2\theta} + \frac{\cot\theta}{\sin\theta} \right). \quad (9b)$$

Finally, in the far field ($r \gg M$) we decompose the dimensionless Weyl scalar $Mr\Psi_4$ as

$$Mr\Psi_4(t, \vec{r}) = \sum_{\ell m} {}_{-2}C_{\ell m}(t) {}_{-2}Y_{\ell m}(\theta, \varphi), \quad (10)$$

where M is the total mass of the binary system (see below for explanations), and r is the radial distance to the binary center of mass. In Eq. (10), and throughout this paper, the notation $\sum_{\ell m}$ is shorthand for $\sum_{\ell=2}^{\infty} \sum_{m=-\ell}^{\ell}$.

B. Details of numerical simulations

We set up the simulations by placing the BHs on an initial Cauchy surface using the Brandt-Brügmann prescription [59]; the Hamiltonian constraint is solved using the second-order-accurate multigrid solver AMRMG [60]. We use the Bowen-York [61] framework to incorporate the BH spins and momenta, with the choice of initial tangential momentum informed by the quasicircular PN approximation of Ref. [38], Eq. (5.3). These initial conditions typically result in a small level of orbital eccentricity, which is quickly damped by the radiation reaction losses. The simulations described in Ref. [12] showed that the final recoil varied by only a few percent over a wider range of initial eccentricities.

The parameters for the runs considered in this paper are shown in Table I. We use the following notation: EQ and NE indicate equal-mass and unequal-mass runs, respectively. The subscripts 0, +, and $-$ refer to zero spin, spin aligned, and spin antialigned with the orbital angular momentum, respectively (the EQ_{planar} run has spins in the orbital plane and antialigned with each other). For the unequal-mass cases we use a superscript to indicate the mass ratio $m_1:m_2$. We denote by m_1 the BH horizon mass computed as

TABLE I. Parameters of the numerical simulations (see Sec. II B for explanations). All masses are normalized to an initial total mass of $M = 1$.

Run	m_1	m_2	δm	q	a_1/m_1	a_2/m_2	Δ^z	Δ^p	ξ^z	Σ_{33}^z	M_f	a_f/M_f	v_f (km/s)
EQ ₊₋	0.503	0.503	0.0	1.0	0.198	-0.198	-0.2	0.0	0.0	0.075	0.967	0.697	90
EQ _{planar}	0.503	0.503	0.0	1.0	0.198	-0.198	0.0	0.2	0.0	0.0	0.967	0.697	690
NE ₀₀ ^{2:3}	0.401	0.593	-0.192	0.677	0.0	0.0	0.0	0.0	0.0	0.0	0.960	0.675	100
NE ₀₀ ^{1:2}	0.333	0.667	-0.333	0.500	0.0	0.0	0.0	0.0	0.0	0.0	0.966	0.633	140
NE ₀₀ ^{1:4}	0.2	0.8	-0.6	0.250	0.0	0.0	0.0	0.0	0.0	0.0	0.980	0.478	150
NE ₊₋ ^{2:3}	0.399	0.610	-0.210	0.655	0.201	-0.194	-0.2	0.0	0.002	0.072	0.971	0.640	190
NE ₊₋ ^{2:3}	0.399	0.610	-0.212	0.653	-0.201	0.193	0.2	0.0	-0.002	-0.072	0.967	0.704	70

$$m_1 = \sqrt{m_{\text{irr},1}^2 + \frac{S_1^2}{4m_{\text{irr},1}^2}}, \quad (11)$$

where $\mathbf{S}_1 = a_1 m_1 \hat{\mathbf{S}}_1 = S_1 \hat{\mathbf{S}}_1$ is the spin angular momentum of BH 1, $m_{\text{irr},1} = \sqrt{A_1/16\pi}$ is its irreducible mass [62], and A_1 is its apparent horizon area. Similar definitions hold for BH 2. The binary's total mass is $M = m_1 + m_2$, $\delta m = m_1 - m_2$, the mass ratio is $q = m_1/m_2 \leq 1$, and the symmetric mass ratio is $\eta = m_1 m_2 / M^2$. Following Kidder [41], we further define the spin vectors $\mathbf{S} = \mathbf{S}_1 + \mathbf{S}_2$, $\mathbf{\Delta} = M(\mathbf{S}_2/m_2 - \mathbf{S}_1/m_1)$, and $\xi = \mathbf{S} + (\delta m/M)\mathbf{\Delta}$. The spin vector Σ_{33}^z is defined below in Sec. VI A.

The mass and spin parameters of the final BH are M_f and a_f . The values of M_f and a_f listed in Table I are computed from the loss of energy and angular momentum from the initial time to the end of the RD phase. They are compatible with the values obtained by extracting the fundamental QNMs (see Sec. IV B below). All spins are orthogonal to the orbital plane, so $\Delta^x = \Delta^y = 0$ (the exception is a single run EQ_{planar} with planar spins discussed in Sec. VI D). In Table I, the spin components in the orbital plane are represented by $\Delta^p \equiv |\Delta^x + i\Delta^y|$. Additionally, all runs have $|a_1|/m_1 = |a_2|/m_2$ with spins pointing in opposite directions, so $\xi \approx 0$ within the accuracy of the initial data.

The simulations were carried out using the moving puncture method [2,3] in the finite-differencing code HAHNDOL [63], which solves the Einstein equations in a standard 3+1 Baumgarte-Shapiro-Shibata-Nakamura (BSSN) [64] conformal formulation. Dissipation [65] terms (tapered to zero near the punctures) and constraint-damping [66] terms were added for robust stability. We used the gauge condition recommended in Ref. [67] for moving punctures, fourth-order-accurate mesh-adapted differencing [68] for the spatial derivatives, and a fourth-order-accurate Runge-Kutta algorithm for the time integration. The adaptive mesh refinement and most of the parallelization was handled by the software package PARAMESH [69], with fifth-order-accurate interpolation between mesh refinement regions.

The grid spacing in the finest refinement region around each BH is $h_f = 3M/160$. We extract data for the radiation

at a radius $r_{\text{ext}} = 45M$. The wave extraction was performed by fourth-order interpolation to a sphere followed by angular integration with a Newton-Cotes formula. We have found satisfactory convergence of the results. For example, for the 1:2 mass-ratio run, for which a higher resolution of $h_f = 1M/64$ was run in addition to $h_f = 3M/160$, the rates of convergence of the Hamiltonian and momentum constraints are comparable to those found in our equal-mass runs reported in [56], and the radiated momenta from the two resolutions agree to within 2%. This was also true for a 2:3 mass-ratio test case with aligned spins (the NE₊₊ run in Ref. [12], which is representative of the NE₊₋^{2:3} and NE₋₊^{2:3} runs here).

III. MULTIPOLAR FORMALISM

In this section we review the most relevant results from Thorne [48], showing how a multipole decomposition of the gravitational radiation field can be used to calculate the energy, angular-momentum, and linear-momentum fluxes from a BH binary system. When restricting the analysis to leading-order terms we shall often express the radiative multipole moments in terms of the source multipole moments [49–52], so in much of the discussion below we will use these two descriptions interchangeably.

A. Linear-momentum flux

In the literature [7–11,15] it is common to compute the linear-momentum flux, and then the recoil, using the following formula:

$$\frac{dP_i}{dt} = \frac{r^2}{16\pi} \int d\Omega \frac{x_i}{r} \left| \int_{-\infty}^t dt \Psi_4 \right|^2, \quad (12)$$

where r is the extraction radius and the antiderivative of Ψ_4 is used because the linear-momentum flux scales as the square of the first derivative of the wave strain, whereas Ψ_4 is proportional to the second derivative of the strain [see Eq. (7) above]. To study how the different multipole moments contribute to the recoil, we could plug Eq. (10) into Eq. (12), as done, e.g., in Ref. [10]. Here, we prefer to use the expression of the linear-momentum flux given in terms

of the symmetric and trace-free (STF) radiative mass and current multipole moments, as done in Refs. [48–52].

Starting from Eq. (4.20') in Ref. [48], we write the linear-momentum flux as

$$F_j \equiv \frac{dP_j}{dt} = \frac{G}{c^7} \sum_{\ell=2}^{\infty} \left[\frac{2(\ell+2)(\ell+3)}{\ell(\ell+1)!(2\ell+3)!!} \times {}^{(\ell+2)}\mathbf{I}_{jA_\ell} {}^{(\ell+1)}\mathbf{I}_{A_\ell} \left(\frac{1}{c}\right)^{2(\ell-2)} + \frac{8(\ell+3)}{(\ell+1)!(2\ell+3)!!} {}^{(\ell+2)}\mathbf{S}_{jA_\ell} {}^{(\ell+1)}\mathbf{S}_{A_\ell} \left(\frac{1}{c}\right)^{2(\ell-1)} + \frac{8(\ell+2)}{(\ell-1)(\ell+1)!(2\ell+1)!!} \epsilon_{jpq} {}^{(\ell+1)}\mathbf{I}_{pA_{\ell-1}} {}^{(\ell+1)}\mathbf{S}_{qA_{\ell-1}} \times \left(\frac{1}{c}\right)^{2(\ell-2)} \right], \quad (13)$$

where \mathbf{I}_{A_ℓ} (\mathbf{S}_{A_ℓ}) are the ℓ -dimensional STF mass (current) tensors and left-hand superscripts represent time derivatives. From these tensors, we can construct the radiative multipole moments $I^{\ell m}$ and $S^{\ell m}$ according to the normalization given by Eq. (4.7) of Ref. [48]:

$$I^{\ell m} = \frac{16\pi}{(2\ell+1)!!} \left(\frac{(\ell+1)(\ell+2)}{2(\ell-1)\ell} \right)^{1/2} \mathbf{I}_{A_\ell} \mathbf{Y}_{A_\ell}^{\ell m*}, \quad (14a)$$

$$S^{\ell m} = \frac{-32\pi\ell}{(\ell+1)(2\ell+1)!!} \left(\frac{(\ell+1)(\ell+2)}{2(\ell-1)\ell} \right)^{1/2} \mathbf{S}_{A_\ell} \mathbf{Y}_{A_\ell}^{\ell m*}, \quad (14b)$$

where $\mathbf{Y}_{A_\ell}^{\ell m}$ are ℓ -dimensional STF tensors that are closely related to the usual scalar spherical harmonics by

$$Y_{\ell m}(\theta, \varphi) = \mathbf{Y}_{i_1 \dots i_\ell}^{\ell m} n^{i_1} \dots n^{i_\ell}, \quad (15)$$

$$F_x^{(1)} + iF_y^{(1)} = \frac{1}{672\pi} [-7i\sqrt{6}S^{32}I^{33*} - 14\sqrt{6}I^{33}I^{44*} - 4\sqrt{21}S^{20}S^{31*} - 4\sqrt{35}S^{21}S^{32*} - 2\sqrt{210}S^{22}S^{33*} + 2\sqrt{42}S^{30}S^{21*} + 14i\sqrt{3}I^{30}S^{31*} - 14i\sqrt{3}S^{30}I^{31*} + 7i\sqrt{10}I^{31}S^{32*} - 7i\sqrt{10}S^{31}I^{32*} - 2\sqrt{105}I^{30}I^{41*} + 6\sqrt{7}I^{40}I^{31*} - 3\sqrt{70}I^{31}I^{42*} + 3\sqrt{14}I^{41}I^{32*} - 21\sqrt{2}I^{32}I^{43*} + 2\sqrt{14}S^{31}S^{22*} + \sqrt{42}I^{42}I^{33*} + 7i\sqrt{6}I^{32}S^{33*}] \quad (19)$$

and

$$F_z^{(1)} = \frac{1}{336\pi} [3\sqrt{7}S^{20}S^{30} + 4\sqrt{14}\text{Re}(S^{21}S^{31*}) + 2\sqrt{35}\text{Re}(S^{22}S^{32*}) - 7\text{Im}(I^{31}S^{31*}) - 14\text{Im}(I^{32}S^{32*}) - 21\text{Im}(I^{33}S^{33*}) + 2\sqrt{21}I^{30}I^{40} + 3\sqrt{35}\text{Re}(I^{31}I^{41*}) + 6\sqrt{7}\text{Re}(I^{32}I^{42*}) + 7\sqrt{3}\text{Re}(I^{33}I^{43*})]. \quad (20)$$

Note that all of the terms in Eqs. (17) and (19) contain products of multipoles with $m' = m \pm 1$, while the terms in Eqs. (18) and (20) have $m' = m$, as with familiar

with $n^i = (\sin\theta \cos\varphi, \sin\theta \sin\varphi, \cos\theta)^i$. Note that the radiative moments $I^{\ell m}$ and $S^{\ell m}$ are scalar quantities and have no explicit spatial dependence. To simplify the notation below, we incorporate the $(\ell+1)$ time derivatives into the radiative multipole moments, and define

$$I^{\ell m} \equiv {}^{(\ell+1)}I^{\ell m}, \quad S^{\ell m} \equiv {}^{(\ell+1)}S^{\ell m}. \quad (16)$$

By combining Eqs. (13), (14), and (16), we find that at leading order (in a $1/c$ expansion) the linear-momentum flux is given by

$$F_x^{(0)} + iF_y^{(0)} = \frac{1}{336\pi} [-14iS^{21}I^{22*} + \sqrt{14}I^{31}I^{22*} - \sqrt{210}I^{22}I^{33*} + 7i\sqrt{6}I^{20}S^{21*} - 7i\sqrt{6}S^{20}I^{21*} + 14iI^{21}S^{22*} + \sqrt{42}I^{30}I^{21*} - 2\sqrt{21}I^{20}I^{31*} - 2\sqrt{35}I^{21}I^{32*}] \quad (17)$$

and

$$F_z^{(0)} = \frac{1}{336\pi} [4\sqrt{14}\text{Re}(I^{31}I^{21*}) - 14\text{Im}(I^{21}S^{21*}) + 2\sqrt{35}\text{Re}(I^{22}I^{32*}) - 28\text{Im}(I^{22}S^{22*}) + 3\sqrt{7}I^{20}I^{30*}]. \quad (18)$$

Note that Eq. (17) coincides with Eq. (9) in Ref. [44] when we equate the radiative multipole moments with the source moments [49–52] and reduce to a circular, nonspinning orbit in the x - y plane. In this case only the first three terms in Eq. (17) survive.

The next-highest-order terms ($1/c^2$ with respect to the leading terms) are proportional to the mass octupoles I^{3m} , or current quadrupoles S^{2m} .

quantum-mechanical operators that involve similar x_i -weighted integrations over the sphere. Also note that for mass-mass and current-current terms, $\ell' = \ell \pm 1$, while for mass-current terms, $\ell' = \ell$.

The above formulas (17)–(20) are valid for completely general orbits, including eccentricity, spin terms, and even for binary systems precessing out of the plane. However, we can simplify them significantly by rotating into the frame where the instantaneous orbital angular momentum is along the z axis. Furthermore, by assuming that terms proportional to \dot{R} (R being the binary radial separation) are negligible, we find $I^{20} = I^{30} = S^{30} = I^{32} = I^{40} = I^{41} = I^{43} = 0$. In the approximation of $\dot{R} = 0$, the inclusion of

terms linear in $\dot{R} \neq 0$ adds no new multipole modes. In fact, one of the primary reasons the derivations above begin with the mass and current tensors \mathbf{A}_{A_ℓ} and \mathbf{S}_{A_ℓ} is to facilitate the calculation of the individual radiative moments $I^{\ell m}$ and $S^{\ell m}$ and also identify the contributions from \dot{R} and \ddot{R} terms from a generalized binary orbit [41]. In the case of nonspinning BHs, the formulas (17)–(20) can be additionally simplified by setting $S^{20} = I^{21} = S^{22} = S^{31} = S^{33} = 0$. Quite interestingly, we obtain that the latter conditions are also valid in the special case of *nonprecessing* BHs where the spins are aligned or antialigned with the orbital angular momentum. Since these are the cases we consider in this paper, we refer often to the following approximate formula for the linear-momentum flux:

$$F_x + iF_y \approx \frac{1}{672\pi} [-28iS^{21}I^{22*} - 2\sqrt{210}I^{22}I^{33*} - 14\sqrt{6}I^{33}I^{44*} + 2\sqrt{14}I^{31}I^{22*} - 7i\sqrt{6}S^{32}I^{33*}], \quad F_z = 0. \quad (21)$$

As we will see below in Sec. IVA, the linear-momentum flux contributions from $I^{31}I^{22*}$ as well as other higher- ℓ modes are typically smaller by at least an order of magnitude. When integrating Eq. (21) to get the recoil velocity, we also find that (due in large part to the relative phases between the modes) the contribution from $S^{32}I^{33*}$ is rather minimal. Thus for most of the analysis that follows, we will focus solely on the first three terms of Eq. (21).

In the following, sometimes we will use

$$\mathbf{F} = \{F_x, F_y, F_z\}, \quad \hat{\mathbf{F}} = \frac{\mathbf{F}}{|\mathbf{F}|}. \quad (22)$$

All the nonprecessing numerical simulations we will analyze have $F_z = 0$, so we can introduce a complex scalar flux

$$F \equiv F_x + iF_y. \quad (23)$$

Since what we extract from the numerical simulations are the modes ${}_{-2}C_{\ell m}$ computed over the sphere surrounding the binary, we need to relate the ${}_{-2}C_{\ell m}$ to the radiative mass and current multipole moments defined above. From Eq. (4.3) of [48],

$$h = \sum_{\ell m} ({}^{(\ell)}I^{\ell m} T_{ab}^{E2, \ell m} m^a m^b + {}^{(\ell)}S^{\ell m} T_{ab}^{B2, \ell m} m^a m^b), \quad (24)$$

where $h \equiv h_{ab} m^a m^b$ and h_{ab} is the metric perturbation $g_{ab} - \eta_{ab}$ in the transverse-traceless gauge, which satisfies Eq. (5), and $T_{ab}^{E2, \ell m}$ and $T_{ab}^{B2, \ell m}$ are the “pure-spin” harmonics of Thorne. From Appendix A of [70],

$$T_{ab}^{E2, \ell m} = \frac{1}{\sqrt{2}} ({}_{-2}Y^{\ell m} m_a m_b + {}_2Y^{\ell m} m_a^* m_b^*), \quad (25a)$$

$$T_{ab}^{B2, \ell m} = \frac{-i}{\sqrt{2}} ({}_{-2}Y^{\ell m} m_a m_b - {}_2Y^{\ell m} m_a^* m_b^*). \quad (25b)$$

Substituting Eqs. (25a) and (25b) into Eq. (24) and recalling that $m^a m_a = 0$ gives

$$h = \frac{1}{\sqrt{2}r} \sum_{\ell m} ({}^{(\ell)}I^{\ell m} + i{}^{(\ell)}S^{\ell m}) {}_{+2}Y^{\ell m}. \quad (26)$$

Now taking the complex conjugate and using the fact that ${}_{+2}Y^{*\ell m} = (-1)^m {}_{-2}Y^{\ell -m}$ [note there is a typo in Eq. (3.1) of Ref. [57]], we obtain

$$h^* = \frac{1}{\sqrt{2}r} \sum_{\ell m} (-1)^m ({}^{(\ell)}I^{\ell m*} - i{}^{(\ell)}S^{\ell m*}) {}_{-2}Y^{\ell -m} \\ = \frac{1}{\sqrt{2}r} \sum_{\ell m} (-1)^m ({}^{(\ell)}I^{\ell -m*} - i{}^{(\ell)}S^{\ell -m*}) {}_{-2}Y^{\ell m}. \quad (27)$$

We decompose the Weyl scalar-strain relation of Eq. (7) into spin-(-2)-weighted spherical harmonics

$$\frac{\partial^2 h^*}{\partial t^2} = -\frac{1}{Mr} \sum_{\ell m} {}_{-2}C_{\ell m -2} Y^{\ell m}, \quad (28)$$

allowing us to see term by term that

$$(-1)^m ({}^{(\ell+2)}I^{\ell -m*} - i{}^{(\ell+2)}S^{\ell -m*}) = -\sqrt{2} {}_{-2}C_{\ell m}. \quad (29)$$

Recall that $(-1)^m I^{\ell -m*} = I^{\ell m}$ and $(-1)^m S^{\ell -m*} = S^{\ell m}$, which allows us to write

$${}^{(\ell+2)}I^{\ell m} = -\frac{1}{\sqrt{2}} [{}_{-2}C_{\ell m} + (-1)^m {}_{-2}C_{\ell -m}^*], \quad (30a)$$

$${}^{(\ell+2)}S^{\ell m} = -\frac{i}{\sqrt{2}} [{}_{-2}C_{\ell m} - (-1)^m {}_{-2}C_{\ell -m}^*]. \quad (30b)$$

Equations (17)–(21) are expressed in terms of $I^{\ell m} \equiv {}^{(\ell+1)}I^{\ell m}$ and $S^{\ell m} \equiv {}^{(\ell+1)}S^{\ell m}$, which can be computed by integrating Eqs. (30a) and (30b) once in time. To avoid the complication of an undetermined constant of integration, we typically integrate ${}_{-2}C_{\ell m}(t)$ *backwards* in time, since in the numerical data (and what we expect happens in reality) all the moments go to zero exponentially after the merger. At early times, on the other hand, most of the modes are significantly nonzero and also include a large amount of numerical noise due to the initial conditions.

B. Energy- and angular-momentum fluxes

Unlike the equations for the linear-momentum flux, which all involve “beating” between pairs of different modes, the energy- and angular-momentum flux expressions involve terms of the form $|I^{\ell m}|^2$, allowing us to isolate the individual contributions from each mode. As we will see below, for the comparable-mass binary systems that we analyze ($m_1:m_2 = 1:1, 2:3, 1:2$), the amplitude of the mass-quadrupole moment I^{22} is roughly an order of magnitude larger than the next largest mode. Thus it almost completely dominates the energy- and angular-momentum fluxes, and we can write [see Eq. (4.16) in Ref. [48]]

$$\frac{dE}{dt} = \frac{1}{32\pi} \sum_{\ell m} (|I^{\ell m}|^2 + |S^{\ell m}|^2) \simeq \frac{1}{16\pi} |I^{22}|^2. \quad (31)$$

The multipole expressions for angular-momentum flux are somewhat more complicated, but for the numerical simulations considered in this paper, the only nonzero modes have $\ell + m$ even for $I^{\ell m}$ and $\ell + m$ odd for $S^{\ell m}$, so we can neglect the $(m, m \pm 1)$ cross terms in Eq. (4.23) of Ref. [48]. These cross terms are responsible for angular-momentum loss in the x - y plane, so it is reasonable that they must be zero for nonprecessing planar orbits. In this case, where the angular momentum is solely along the \hat{z} axis, we have

$$\begin{aligned} \frac{dJ_z}{dt} &= \frac{i}{32\pi} \sum_{\ell m} m^{(\ell)} I^{\ell m*} I^{\ell m} + (\ell) S^{\ell m*} S^{\ell m} \\ &\simeq -\frac{1}{8\pi} \text{Im}[(^{(2)}I^{22*} (^{(3)}I^{22})], \end{aligned} \quad (32)$$

where we have restored the explicit time derivatives as in Eq. (16).

Integrating Eqs. (31) and (32) term by term, we can calculate how much energy and angular momentum are radiated in each of the dominant modes, similar to the approach of Ref. [71]. We introduce the quantities $E_{\ell m}$ and $J_{\ell m}$ as the total energy and angular momentum radiated in each (ℓ, m) mode, computed by integrating Eqs. (31) and (32) in time, term by term (for conciseness, we combine both the m and $-m$ terms into $E_{\ell m}$ and $J_{\ell m}$ and restrict our notation to $m > 0$). Note that while $E_{\ell m}$ is always positive, $J_{\ell m}$ can also be negative, corresponding to angular momentum in the $-\hat{z}$ direction. These results are shown in Table II, along with the contributions from just the RD phase ($t > t_{\text{peak}}$, where t_{peak} is the point at which $|I^{22}|$ reaches its peak, closely corresponding to the peak in GW energy emission). We will see below in Sec. V that these various energy contributions agree closely with the Newtonian predictions for the relative mass scalings. For example, the energy E_{22} in the inspiral phase should scale as η , while the RD contribution should scale like η^2 . It is important to note that the different moments have different scalings: $E_{33} \sim \eta^2 \delta m^2$, while the I^{44} contribution has a much weaker dependence on the mass ratio: $E_{44} \sim \eta^2 (1 - 3\eta)^2$.

In the limit of very large initial separation (small initial frequency), each of the $E_{\ell m}$ and $J_{\ell m}$ should converge to a finite value, with the notable exception of J_{22} . It is well known that the angular momentum of a binary system scales as $R^{1/2}$, and is thus unbound in the limit of $R \rightarrow \infty$, but it is interesting to see that the higher-order contributions to the angular momentum all converge at large R . This can be understood directly from Eq. (32) in the Keplerian limit of $R = M^{1/3} \omega^{-2/3}$. At leading order, radiation reaction follows the relation $dt \sim \omega^{-11/3} d\omega$, so the angular momentum in the inspiral is

$$\begin{aligned} J_{22} &= \frac{1}{8\pi} \int_{t=-\infty}^{t_0} dt \text{Im}[(^{(2)}I^{22*} (^{(3)}I^{22})] \\ &\sim \int_{\omega=0}^{\omega_0} \omega^{2/3} \omega^{5/3} \omega^{-11/3} d\omega \rightarrow \infty. \end{aligned} \quad (33)$$

As we will see below in Sec. V, for all the other energy- and angular-momentum modes, the fluxes from Eqs. (31) and (32) scale as $\omega^{10/3}$ or higher powers, and thus converge when integrated over $\omega^{-11/3} d\omega$.

IV. MULTIPOLE ANALYSIS OF THE NUMERICAL SIMULATIONS

In this section we want to investigate how the different multipole moments evolve during the inspiral and ring-down phases of BH binary mergers.

A. Inspiral phase

As can be derived in PN theory [33] and has been confirmed numerically in Refs. [2,3], the $\ell = 2, m = 2$ mode in Eq. (10) is circularly polarized to leading order throughout the coalescence. Because of this, Ref. [72] defined the (dominant) orbital angular frequency as

$$\omega_D^{\ell m} = -\frac{1}{m} \text{Im} \left(\frac{-2\dot{C}_{\ell m}}{-2C_{\ell m}} \right). \quad (34)$$

Here, we extend Eq. (34) by defining several (dominant) orbital angular frequencies, each of them being related to a specific multipole moment, $I^{\ell m}$ or $S^{\ell m}$, as

TABLE II. Energy and angular momentum radiated in each of the dominant multipole modes. In parentheses we show the amount radiated only after the peak of GW energy flux. All units are normalized to $M = 1$.

Run	$E_{22} (\times 10^{-2})$	$E_{21} (\times 10^{-4})$	$E_{32} (\times 10^{-4})$	$E_{33} (\times 10^{-4})$	$E_{44} (\times 10^{-4})$	$J_{22} (\times 10^{-1})$	$J_{21} (\times 10^{-4})$	$J_{32} (\times 10^{-4})$	$J_{33} (\times 10^{-3})$	$J_{44} (\times 10^{-3})$
EQ ₊₋	3.5 (1.4)	0.22 (0.17)	1.6 (1.2)	0.04 (0.02)	3.3 (1.5)	2.2 (0.50)	-0.70 (-0.46)	7.9 (-2.0)	-0.02 (-0.01)	1.9 (0.64)
NE ₀₀ ^{2:3}	3.1 (1.1)	0.61 (0.40)	0.90 (0.66)	5.6 (2.8)	2.9 (1.0)	2.2 (0.45)	-2.1 (-0.98)	3.9 (2.5)	-3.1 (-1.1)	1.8 (0.46)
NE ₀₀ ^{1:2}	2.5 (0.87)	1.4 (0.94)	0.47 (0.30)	12.0 (5.8)	2.7 (0.73)	1.8 (0.37)	-4.8 (-2.4)	2.4 (1.3)	-6.9 (-2.3)	1.7 (0.30)
NE ₀₀ ^{1:4}	1.2 (0.35)	2.1 (1.4)	0.27 (0.09)	16.0 (6.6)	3.3 (1.2)	1.2 (0.16)	-8.0 (-3.8)	1.6 (0.27)	-11.0 (-2.9)	2.4 (0.48)
NE ₊₋ ^{2:3}	2.9 (1.0)	1.6 (1.0)	0.93 (0.67)	5.2 (2.5)	2.6 (0.82)	2.0 (0.31)	-5.4 (-2.9)	2.1 (5.3)	-2.9 (-0.98)	1.6 (0.33)
NE ₊₋ ^{2:3}	3.3 (1.1)	0.14 (0.09)	1.1 (0.78)	7.1 (3.4)	2.9 (0.92)	2.3 (0.44)	-0.50 (-0.21)	4.4 (3.1)	-3.9 (-1.3)	1.8 (0.37)

$$\omega_D^{I\ell m} = -\frac{1}{m} \text{Im}\left(\frac{\dot{I}^{\ell m}}{I^{\ell m}}\right), \quad \omega_D^{S\ell m} = -\frac{1}{m} \text{Im}\left(\frac{\dot{S}^{\ell m}}{S^{\ell m}}\right). \quad (35)$$

We plot these frequencies in Fig. 2 for the dominant multipole moments I^{22} , S^{21} , I^{33} , I^{44} , and S^{32} , for the $\text{NE}_{00}^{2:3}$ (left panel) and $\text{NE}_{00}^{1:2}$ (right panel) runs. The amplitudes of the I^{31} and I^{42} modes are too weak and dominated by noise to extract a dominant frequency. In this figure, as well as most shown in the rest of the paper, we plot the time variable with respect to t_{peak} . We notice that the frequencies corresponding to the modes with $\ell = m$ agree quite well throughout the inspiral and ringdown phases, but the frequency of the S^{21} mode decouples from the others approximately $50M$ before the peak in the I^{22} mode. As we shall see in Sec. VI, this is due to the fact that, during the ringdown phase, the dominant angular frequency associated to the S^{21} mode is almost twice as large as those of the other leading modes [73–75]. This decoupling plays a major role in determining the shape of the kick and anti-kick (see Sec. VI below), and also suggests that the transition to RD may begin long before the peak of the GW flux. Similarly, the S^{32} mode should converge to a higher RD frequency ($\omega_{320}/2 \simeq 0.37/M_f$ for these runs), but may be limited by numerical noise here, as well as possible mode mixing with the dominant I^{22} moment.

In Fig. 3 we show the amplitudes of the multipole moments in Eq. (21). Again, the left panel refers to the $\text{NE}_{00}^{2:3}$ run, while the right panel refers to the $\text{NE}_{00}^{1:2}$ run. The mass-quadrupole moment I^{22} clearly dominates in both cases, while the I^{31} and I^{42} modes are so weak as to be almost completely overwhelmed by numerical noise. In addition to having dissimilar amplitudes, the different moments also peak at slightly different times, which may be related to the

fact that RD modes are excited at different times. In particular, the modes mentioned above with $\ell \neq m$ tend to peak later in time, perhaps due to a longer transition to the higher QNM frequency. As we shall see in Sec. V, as the mass ratio becomes more extreme (i.e., decreasing η), the higher-order modes increase in relative amplitude, with I^{33} and S^{21} both proportional to $\eta\delta m$. I^{44} and S^{32} , however, scale as $\eta(1 - 3\eta)$, so they increase only slightly in the range of masses considered here.

Next, in Fig. 4, we show the amplitude of the linear-momentum flux from the mode pairs included in Eq. (21). Here we define the complex flux $F^{21,22} = (-14i/336\pi) \times S^{21} I^{22*}$ and other $F^{\ell m, \ell' m'}$ analogously from Eq. (21). As in Fig. 3, the mass-quadrupole terms dominate, with significantly smaller contributions from the S^{32} and I^{31} modes. However, note the appreciable flux amplitude from the $F^{33,44} \sim I^{33} I^{44*}$ term, which is formally a higher-order correction in a $(1/c)$ expansion [43,44]. From Fig. 4, we expect that the first three pairs of modes in Eq. (21) should contribute most significantly to the recoil. Including the complex phase relations between the different modes, we find that this result will be supported further by the analysis in Sec. VIA.

B. Ringdown phase

We now extract the QNMs, notably the fundamental and the first two overtones, present in the most significant multipole moments during the RD phase. We follow the procedure outlined in Ref. [72]. To avoid possible constant offsets introduced by integrating Eqs. (30a) and (30b), we prefer to extract the QNMs directly from the ${}_{-2}C_{\ell m}$ instead of using $I_{\ell m}$ or $S_{\ell m}$. Additionally, from Eqs. (30a) and (30b), we see that ${}^{(1)}I^{\ell m}$ and ${}^{(1)}S^{\ell m}$ are made up of both ${}_{-2}C_{\ell m}$ and ${}_{-2}C_{\ell -m}$, which, in general, do not have the

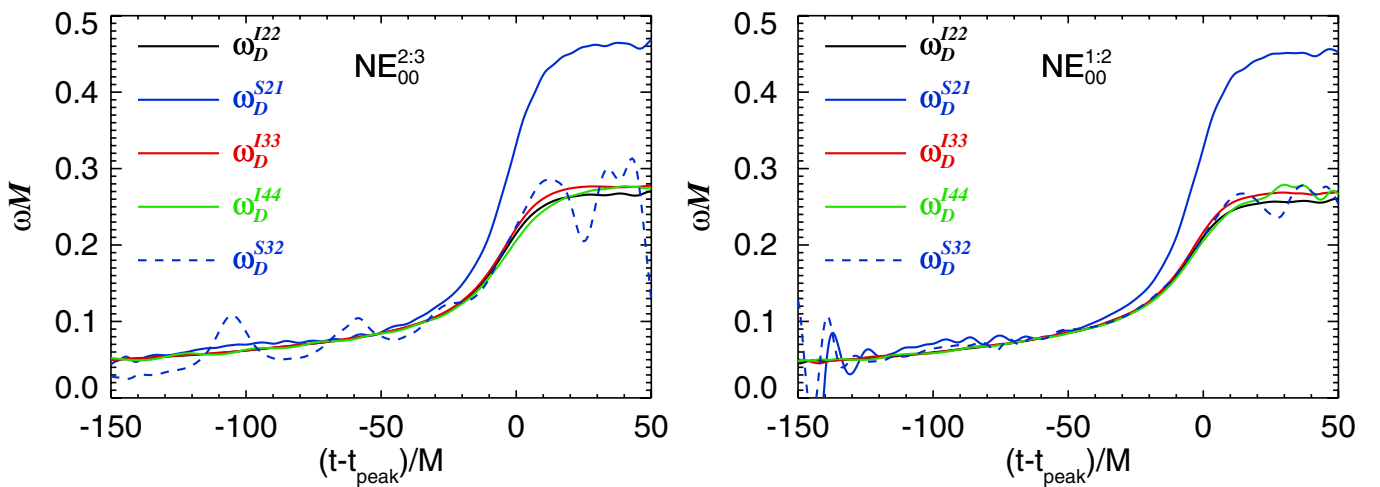


FIG. 2 (color online). Dominant orbital angular frequency obtained from the individual radiative multipole moments, as determined by Eq. (35). The different frequencies with $\ell = m$ agree closely throughout the inspiral and RD phases. The frequency with $\ell = 2$, $m = 1$ decouples from the others at earlier time and reaches a much higher plateau. The left panel refers to the $\text{NE}_{00}^{2:3}$ run and the right panel to the $\text{NE}_{00}^{1:2}$ run. We denote with t_{peak} the time at which I^{22} reaches its maximum.

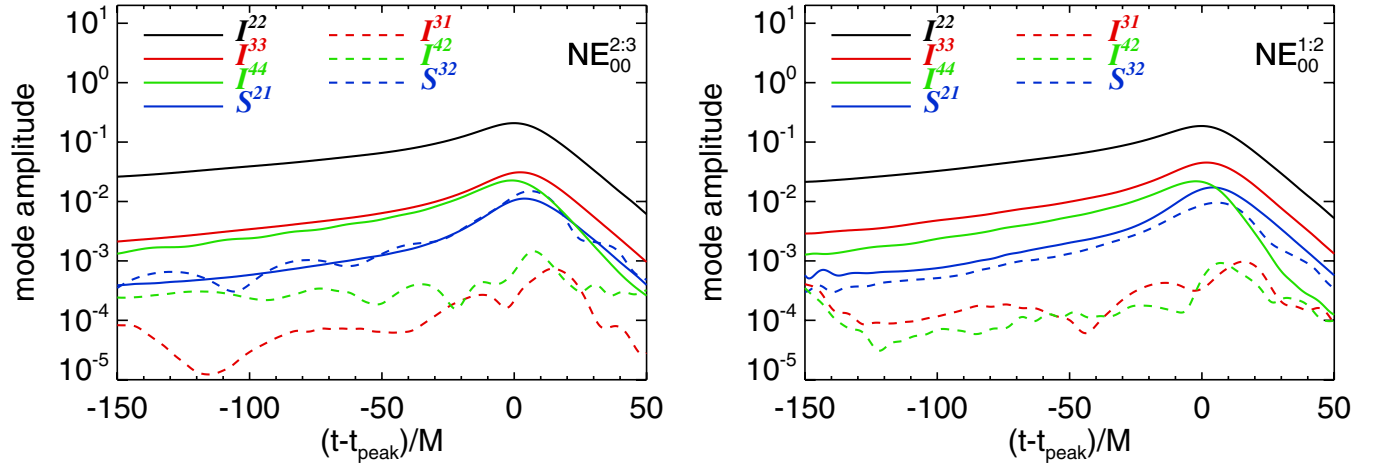


FIG. 3 (color online). Amplitudes of the dominant radiative multipole moments. On the left panel we show the modes for the $\text{NE}_{00}^{2:3}$ run, while on the right panel we show the modes for the $\text{NE}_{00}^{1:2}$ run. The leading-order mass quadrupole I^{22} is about an order of magnitude stronger than any other mode. The oscillating behavior of the S^{32} moment during RD is likely due to mode-mixing with I^{22} . We denote with t_{peak} the time at which I^{22} reaches its maximum.

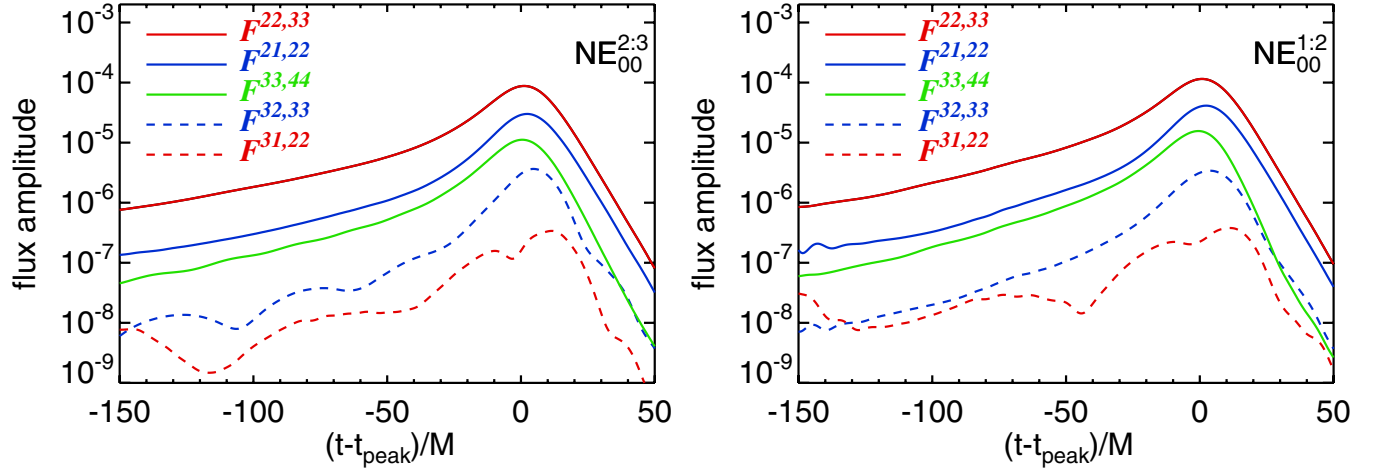


FIG. 4 (color online). Linear-momentum flux of the strongest radiative multipole moments, i.e., the ones in Eq. (21). On the left panel we show the modes for the $\text{NE}_{00}^{2:3}$ run, while on the right panel we show the modes for the $\text{NE}_{00}^{1:2}$ run. We denote with t_{peak} the time at which I^{22} reaches its maximum.

same QNM frequencies, so it is more reliable to extract the RD modes from just ${}_{-2}C_{\ell m}$ (however, in practice we find that the RD phase is dominated by modes with positive m). Following the approach of Ref. [75], we define the complex frequencies $\sigma_{\ell mn}$:

$$\sigma_{\ell mn} \equiv \omega_{\ell mn} - i/\tau_{\ell mn}, \quad (36)$$

and each RD mode is proportional to $\exp(-i\sigma_{\ell mn}t)$. In this notation, $\omega_{\ell mn}$ are the QNM oscillation frequencies [not to be confused with the dominant frequencies of Eq. (35)] and $\tau_{\ell mn}$ are the mode decay times, all functions of the final black hole mass and spin. The subscripts ℓ and m are the same spherical wave numbers used above, and $n = 0$ denotes the fundamental mode, with $n = 1, 2, \dots$, corre-

sponding to the higher overtones. The fundamental QNM frequencies $\sigma_{\ell m0}$ are listed in Table III for the NR runs listed above. All frequencies and decay times are measured in units of the final mass M_f .

We present the RD analysis only for the $\text{NE}_{00}^{2:3}$ run, but the others are qualitatively very similar. We have extracted the various QNM contributions to the ${}_{-2}C_{\ell m}$ RD signal in the following way (see also Ref. [72]): We expect that at late times the $n = 0$ QNM dominates. We fit the signal after time $t_{\text{peak}} + t_r$ to this single mode using nonlinear regression and choose t_r to minimize the error in the fit. We have four dimensionless parameters in this nonlinear fit: the QNM amplitude and phase, $\mathcal{C}_{\ell m0}$ and $\phi_{\ell m0}$, and the QNM frequency and decay time, $M\omega_{\ell m0}$ and $\tau_{\ell m0}/M$.

TABLE III. Frequencies and decay times for the fundamental QNMs for each of the numerical simulations. $\omega_{\ell m 0}$ is in units of M_f^{-1} , and $\tau_{\ell m 0}$ is in units of M_f .

Run	a_f/M_f	ω_{210}	τ_{210}	ω_{220}	τ_{220}	ω_{320}	τ_{320}	ω_{330}	τ_{330}	ω_{440}	τ_{440}
EQ ₊₋	0.697	0.454	12.2	0.531	12.4	0.758	11.9	0.841	12.0	1.14	11.8
NE ₀₀ ^{2:3}	0.675	0.450	12.1	0.521	12.2	0.749	11.7	0.827	11.9	1.12	11.7
NE ₀₀ ^{1:2}	0.633	0.442	11.9	0.505	12.1	0.734	11.6	0.803	11.7	1.09	11.5
NE ₀₀ ^{1:4}	0.423	0.411	11.5	0.445	11.5	0.674	11.1	0.711	11.1	0.963	10.9
NE ₊₋ ^{2:3}	0.640	0.443	11.9	0.507	12.1	0.736	11.6	0.806	11.7	1.09	11.5
NE ₊₋ ^{2:3}	0.704	0.456	12.2	0.533	12.4	0.760	11.9	0.845	12.1	1.14	11.9

However, instead of fitting directly for these four parameters, we treat $M\omega_{\ell m 0}$ and $\tau_{\ell m 0}/M$ as functions of a_f/M_f and M_f/M (which can be obtained via interpolation from tabulated values given in Ref. [75]). The advantage of using $(a_f/M_f, M_f/M, \mathcal{C}_{\ell m 0}, \phi_{\ell m 0})$ for the set of fitting parameters comes when we fit to higher overtones. As done in Ref. [72], we extract the QNMs treating the real and imaginary parts of ${}_{-2}\mathcal{C}_{\ell m}$ as independent. Below we shall list results obtained from $\text{Re}[{}_{-2}\mathcal{C}_{\ell m}]$.

By applying this procedure to the dominant mode, ${}_{-2}\mathcal{C}_{22}$, we obtain $a_f/M_f = 0.669$ and $M/M_f = 0.965$ together with the amplitude and phase of the fundamental QNM. We include additional overtones ($n > 0$) successively. For each value of n , we refit the entire function, so for $n = 0$ there are four parameters in the fit, for $n = 1$ there are six, for $n = 2$ there are eight, and so forth. Thus, applying a six-parameter fit, we successfully extract also the first overtone simultaneously, obtaining slightly differ-

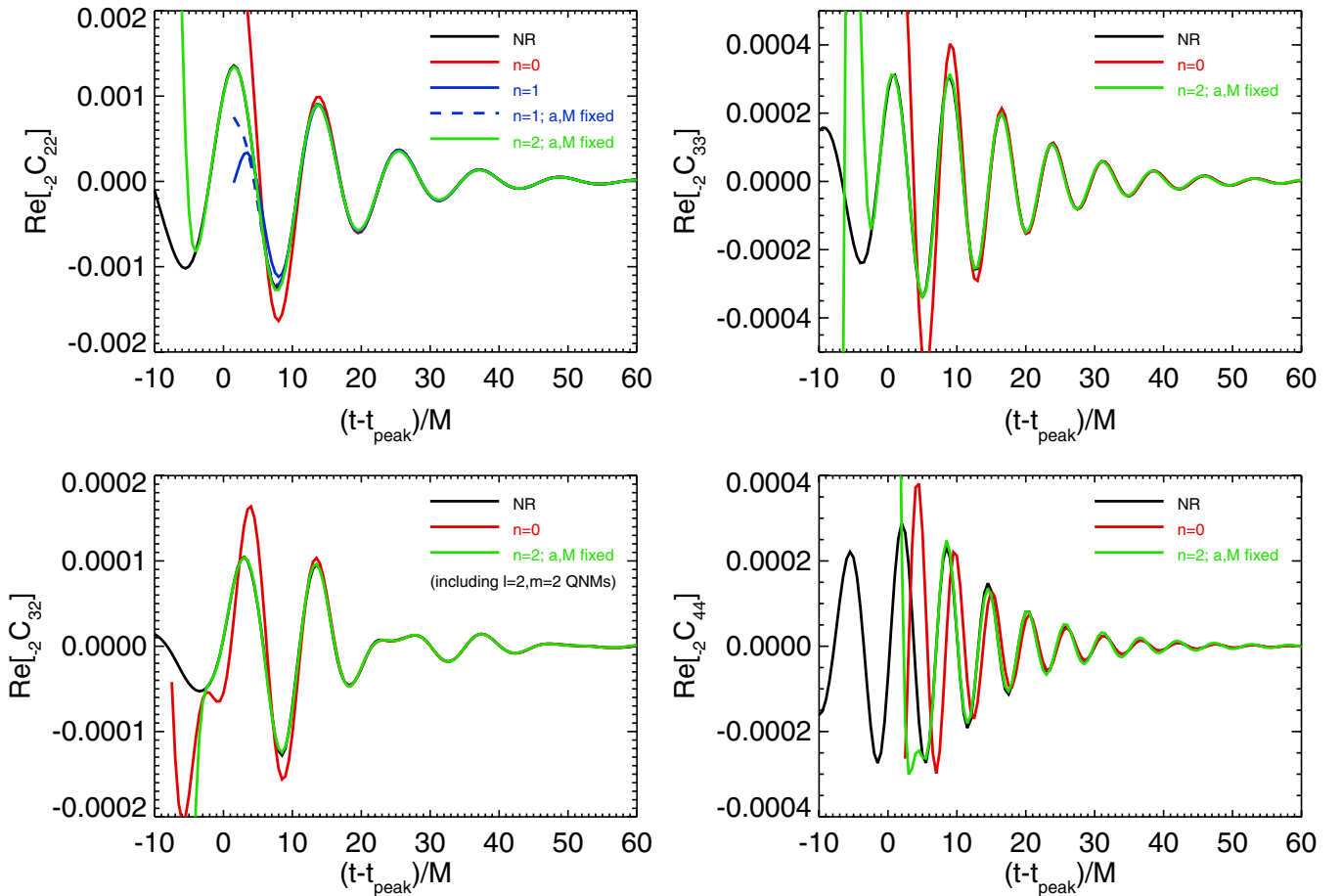


FIG. 5 (color online). Comparison of numerical and QNM waveforms for the NE₀₀^{2:3} run. The dominant modes analyzed are ${}_{-2}\mathcal{C}_{22}$ (upper left panel), ${}_{-2}\mathcal{C}_{33}$ (upper right panel), ${}_{-2}\mathcal{C}_{32}$ (lower left panel), and ${}_{-2}\mathcal{C}_{44}$ (lower right panel). Note that the ${}_{-2}\mathcal{C}_{32}$ waveform includes contributions from the $\ell = 2, m = 2$ modes as well. We denote with t_{peak} the time of the peak of I^{22} .

ent values for $a_f/M_f = 0.661$ and $M/M_f = 0.958$. We find it impossible, however, to extract the second overtone with a single eight-parameter fit. By contrast, if we keep a_f/M_f and M/M_f fixed and equal to the values obtained when extracting the fundamental QNM, we find that we can fit up to the second overtone. Moreover, quite interestingly, the fit provides waveforms that compare very well with the NR waveforms up to the peak of I_{22} , as can be seen in the upper left panel of Fig. 5.

The remaining panels in Fig. 5 show results for the other relevant modes ${}_{-2}C_{33}$, ${}_{-2}C_{44}$, and ${}_{-2}C_{32}$. As obtained in Ref. [72], we find a “mode-mixing” in ${}_{-2}C_{32}$, i.e., the RD waveform is a combination of $\ell = 2$, $m = 2$ and $\ell = 3$, $m = 2$ QNMs. This effect appears to be most important between modes with the same m value, and may possibly be explained by the fact that the QNMs should really be expressed as *spheroidal*, not *spherical* harmonics [72,75]. Including both sets of modes means that the ${}_{-2}C_{32}$ is actually fit using 14 parameters: the final mass and spin, and the amplitude and phase of six QNMs.

By fitting the fundamental QNM for each ringdown waveform, we obtain $a_f/M_f = 0.671$ and $M/M_f = 0.972$; $a_f/M_f = 0.527$ and $M/M_f = 0.884$; $a_f/M_f = 0.686$ and $M/M_f = 0.981$, for ${}_{-2}C_{33}$, ${}_{-2}C_{44}$, and ${}_{-2}C_{32}$, respectively. We also are able to extract the fundamental QNM for the ${}_{-2}C_{21}$ mode (not shown in Fig. 5) and find $a_f/M_f = 0.678$ and $M/M_f = 0.960$. All of these values for the inferred final BH spin and mass are rather consistent, except for ${}_{-2}C_{44}$. This discrepancy might be due to numerical resolution effects, and will be the subject of future investigations.

Thus we find that, although we cannot simultaneously extract three QNMs (the fundamental and two overtones) and we are not able to clearly determine the onset of the RD phase, we *do* obtain that for $t > t_{\text{peak}}$ the numerical waveforms can be well fitted by a superposition of three QNMs. This result explains why the simple matching procedure from inspiral to RD adopted in the EOB model [36,44,72] can almost always work successfully (see Ref. [76] for some caveats). In Sec. VB we shall adopt the same matching procedure of the EOB model when building the full waveform using the pseudoanalytic model of Sec. V.

V. EFFECTIVE NEWTONIAN MODEL

In an attempt to better understand the amplitudes and frequencies of the various modes during the inspiral and merger phases, we present here what we call the “effective Newtonian” (eN) model. It begins with calculating the leading-order Newtonian formulas for each multipole moment of the source, as a function of the BH masses, binary separation R , and orbital phase ϕ . To extend these formulas through the end of the inspiral and into the merger phase, we introduce an effective radial separation to absorb PN effects into the leading-order multipole expressions.

Each multipole moment is then individually matched to a linear superposition of ringdown modes, as is done in the effective-one-body model [36,44,72]. Taken together with the match to Kerr QNMs, this eN model provides an excellent framework within which we can understand the details of the linear-momentum flux and net recoil velocity.

A. Newtonian multipole moments

Working at leading Newtonian order for each mode, we equate the radiative multipole moments to the source multipole moments. Restricting ourselves to circular, planar orbits, we find that for nonspinning systems, the dominant modes are [49–52]

$$S_{\text{no spin}}^{21} = -\frac{8}{3}i\sqrt{\frac{2\pi}{5}}\frac{\delta m}{M}\mu R^3\omega^4 e^{-i\phi}, \quad (37a)$$

$$I_{\text{no spin}}^{22} = 16i\sqrt{\frac{2\pi}{5}}\mu R^2\omega^3 e^{-2i\phi}, \quad (37b)$$

$$I_{\text{no spin}}^{31} = -\frac{2}{3}\sqrt{\frac{\pi}{35}}\frac{\delta m}{M}\mu R^3\omega^4 e^{-i\phi}, \quad (37c)$$

$$S_{\text{no spin}}^{32} = -\frac{16}{3}\sqrt{\frac{2\pi}{7}}\mu(1-3\eta)R^4\omega^5 e^{-2i\phi}, \quad (37d)$$

$$I_{\text{no spin}}^{33} = 54\sqrt{\frac{\pi}{21}}\frac{\delta m}{M}\mu R^3\omega^4 e^{-3i\phi}, \quad (37e)$$

$$I_{\text{no spin}}^{42} = \frac{16}{63}i\sqrt{2\pi}\mu(1-3\eta)R^4\omega^5 e^{-2i\phi}, \quad (37f)$$

$$I_{\text{no spin}}^{44} = -\frac{256}{9}i\sqrt{\frac{2\pi}{7}}\mu(1-3\eta)R^4\omega^5 e^{-4i\phi}, \quad (37g)$$

where R is the radial separation and $\omega = \dot{\phi}$ is the binary orbital frequency. Considering only the mass-quadrupole terms in the linear-momentum flux (i.e., the terms proportional to $S^{21}I^{22*}$, $I^{31}I^{22*}$, and $I^{22}I^{33*}$), we obtain the well-known result valid at Newtonian order [44]:

$$F^{(0)} = -i\frac{464}{105}\frac{\delta m}{M}\mu^2 R^5 \omega^7 e^{i\phi}. \quad (38)$$

Including the next-highest-order moments in Eq. (19), we get

$$F^{(1)} = -i\frac{11\,120}{1323}\frac{\delta m}{M}\mu^2(1-3\eta)R^7\omega^9 e^{i\phi}. \quad (39)$$

While there may also be next-to-leading-order contributions from a PN expansion of the multipole moments included in Eq. (17) that would show up in Eq. (39), we can effectively absorb those corrections into the R variable, as will be described below.

Combining Eqs. (38) and (39) we find the linear-momentum flux scales like

$$|F^{(0)} + F^{(1)}| \propto \frac{\delta m}{M} \mu^2 \left[1 + \frac{3475}{1827} (1 - 3\eta) R^2 \omega^2 \right] \approx \frac{3}{2} \frac{\delta m}{M} \mu^2 (1 - 0.9\eta), \quad (40)$$

which is remarkably similar to the result found in Ref. [9]. Here we have used $R^2 \omega^2 \approx 0.23\text{--}0.25$ at the peak of the energy flux, which seems to be quite robust for a range of mass ratios. However, the extremely close agreement with Ref. [9] is probably to some degree a coincidence, since this simple Newtonian formula does not include any details of the phase relations between different modes, which become especially important during the transition from inspiral to ringdown (see Sec. VIB below). Since Eq. (40) really only applies to the inspiral portion, if anything, it should be a predictor of how the *peak* recoil velocity scales. This is not necessarily the same as the *final* recoil, since we find that more extreme mass-ratio BH binaries have a relatively smaller antikick, which should also play an important role in the scaling relation of Ref. [9].

If we compute the above multipole moments (37a)–(37g) using ω as given by Eq. (35) and R as obtained from the puncture trajectories, we do not find a very good agreement with the numerical results. This is not surprising since there is no reason to believe that the Newtonian approximation should work well all along the inspiral phase. We should expect that higher-order PN corrections become important as we approach the merger. Furthermore, R is a coordinate-dependent quantity, and thus does not necessarily have the same meaning in a PN expression as in NR. Since our scope is limited to a

diagnostic of the NR results, and not to a precise comparison with PN calculations, instead of including PN corrections in Eqs. (37)–(39), we investigate whether by properly scaling the Newtonian expressions we can get a better agreement until the merger. We can also think of this normalization as a way of resumming the PN expansion.

Quite interestingly, if we compute the amplitudes $|I^{\ell m}|$ or $|S^{\ell m}|$ from the numerical data, and the angular frequency ω from Eq. (35), we find that the radii $R^{\ell m}$ which appear in the right-hand side of Eqs. (37a)–(37g) are rather independent of the multipole moments ℓ and m , as Fig. 6 shows. We denote the radii $R^{\ell m}$ computed numerically as *effective radii* $R_{\text{eff}}^{\ell m}$. The close agreement between the frequencies (see Fig. 2) and effective radii for each mode suggests we can use the Newtonian expressions and a single $R_{\text{eff}}(t)$ and orbital frequency $\omega(t)$, e.g., $R_{\text{eff}}^{22}(t)$ and ω_D^{22} for all modes with a high degree of accuracy for the entire inspiral phase and even during the transition to merger.

For comparison we also show in Fig. 6 the radius from the puncture trajectory (dot-dashed curves) and the radius computed using the Arnowitt-Deser-Misner (ADM) transverse-traceless gauge (dashed curves), given as a function of frequency through 3PN order by [77]

$$R_{\text{ADM}} = M^{1/3} \omega^{-2/3} \left[1 + \omega^{2/3} \left(-1 + \frac{\eta}{3} \right) + \omega^{4/3} \left(-\frac{1}{4} + \frac{9}{8} \eta + \frac{\eta^2}{9} \right) + \omega^2 \left(-\frac{1}{4} - \frac{1625}{144} \eta + \frac{167}{192} \eta \pi^2 - \frac{3}{2} \eta^2 + \frac{2}{81} \eta^3 \right) \right]. \quad (41)$$

Here we use the orbital frequency ω derived from the I^{22}

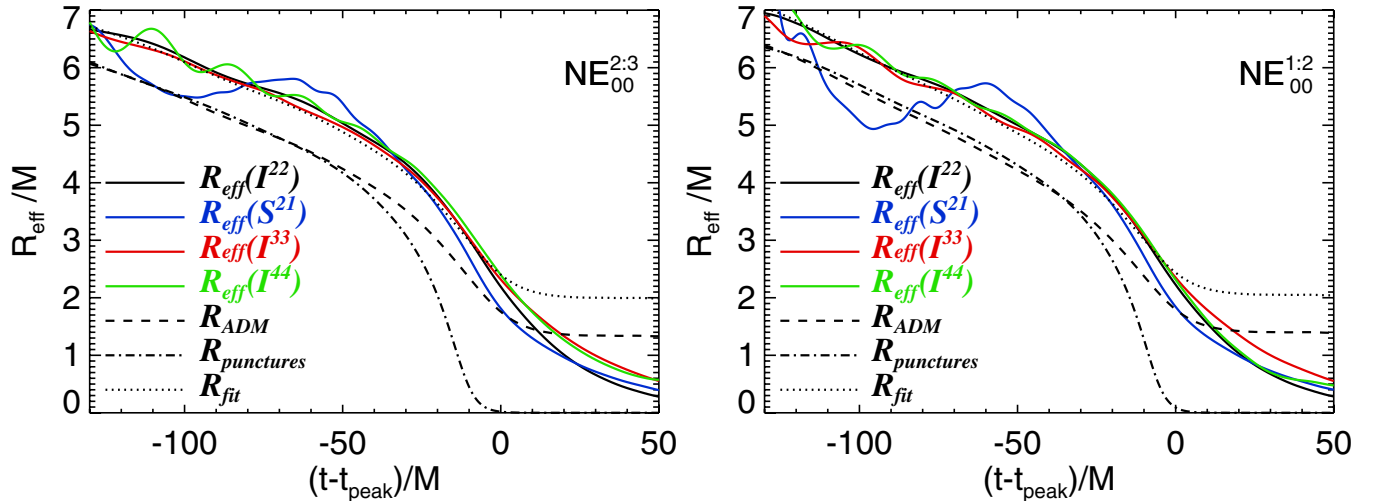


FIG. 6 (color online). Effective radius for different modes, derived from Eqs. (35) and (37a)–(37g). The close agreement for the R_{eff}^{lm} suggests we can use a single effective radius $R_{\text{eff}}(t)$ for the Newtonian expressions. We believe that the large oscillations in R_{eff}^{21} are due to initial eccentricity at early times. Also plotted is the ADM radius (dashed curves) derived from the orbital frequency via Eq. (41), the coordinate separation of the BH punctures (dot-dashed curves), and the empirical fit R_{fit} (dotted curves) obtained by shifting R_{ADM} by 0.65. The results correspond to the $\text{NE}_{00}^{2:3}$ (left panel) and $\text{NE}_{00}^{1:2}$ (right panel) runs. We denote with t_{peak} the time at which I^{22} reaches its maximum.

mode via Eq. (35), giving a constant value during the RD phase when the orbital frequency is meaningless. Figure 6 shows interesting agreement between R_{ADM} and the radius from the puncture trajectory, and a constant offset between R_{ADM} and R_{eff} . The latter is due to the fact that the amplitude of the multipole moments computed at leading Newtonian order does not reproduce the numerical relativity amplitude [56,72], and higher-order PN corrections need to be included. Motivated by this similarity between R_{ADM} and R_{eff} , we attempt to fit empirically the R_{eff} curves in Fig. 6 by simply shifting R_{ADM} by 0.65. The fit curve is included as a dotted curve in Fig. 6. As we accumulate longer and more accurate NR data for a wider range of η values, and study possible analytic resummation of higher-order PN amplitude corrections, we should be able to work out a widely applicable amplitude-scaling factor to be included in leading-order analytic waveforms [76].

In the next section, we shall investigate how this simple eN model can be combined with a superposition of QNMs, as described in Sec. IV B, giving a good representation of the NR results.

B. Matching to ringdown

We now match the inspiral and RD waveforms in a mode-by-mode fashion following the philosophy of the EOB approach [36]. Note this is not the same analysis of Sec. IV B, where we *fit* the numerical data throughout the RD phase with a superposition of QNMs. Here we *match* the data at a single point at the transition from inspiral to RD and see how well it agrees with the rest of the RD phase. A similar attempt was followed in Ref. [44], where for simplicity the authors performed the matching to the Schwarzschild QNM frequencies, while we use the Kerr QNM frequencies and match to the fundamental QNM frequency and the first two overtones, as done in Ref. [72]. We obtain the QNM frequencies and decay times from Ref. [75] as a function of a_f/M_f (taken from Table I above). For the fundamental and two overtone QNMs, we can match a given multipole mode by equating it and two time derivatives to a linear combination of QNMs.

We write

$$I^{\ell m}(t) = A(t)e^{-i\phi(t)} = \sum_{n=0}^{\infty} A_{\ell mn} e^{-i\sigma_{\ell mn}(t-t_{\text{match}})}, \quad (42)$$

where the complex QNM frequencies are known functions of the final BH mass and spin, and we must solve for the complex amplitudes $A_{\ell mn}$. Matching three QNMs we get

$$I^{\ell m}(t_{\text{match}}) = \sum_{n=0}^2 A_{\ell mn}, \quad (43a)$$

$$\frac{d}{dt} I^{\ell m}(t_{\text{match}}) = -i \sum_{n=0}^2 \sigma_{\ell mn} A_{\ell mn}, \quad (43b)$$

$$\frac{d^2}{dt^2} I^{\ell m}(t_{\text{match}}) = - \sum_{n=0}^2 \sigma_{\ell mn}^2 A_{\ell mn}, \quad (43c)$$

or as a simple matrix equation

$$\begin{pmatrix} 1 & 1 & 1 \\ -i\sigma_{\ell m0} & -i\sigma_{\ell m1} & -i\sigma_{\ell m2} \\ -\sigma_{\ell m0}^2 & -\sigma_{\ell m1}^2 & -\sigma_{\ell m2}^2 \end{pmatrix} \begin{pmatrix} A_{\ell m0} \\ A_{\ell m1} \\ A_{\ell m2} \end{pmatrix} = \begin{pmatrix} I^{\ell m} \\ \dot{I}^{\ell m} \\ \ddot{I}^{\ell m} \end{pmatrix}. \quad (44)$$

In Fig. 7, we compare the NR modes to the modes obtained by the effective Newtonian model described in Sec. VA until t_{match} and by the superposition of three QNMs for $t > t_{\text{match}}$. During the inspiral, the different moments are calculated according to Eqs. (37a)–(37g), using a single R_{eff} and ω_D determined from the I^{22} mode, with the exception of the S^{21} mode, where we instead use the higher frequency ω_D^{S21} (but the same R_{eff}). We treat t_{match} as a free parameter: if we stop the inspiral too early, the eN mode amplitudes are still growing, so the sudden transition to decaying RD modes prematurely reduces them. On the other hand, if the inspiral is continued too long, we tend to lose the important phase shifts between the modes that only begin during the transition to RD. This is particularly evident in the I^{44} mode, which undergoes an unexplained phase shift around the transition to RD, and also decays at a somewhat different rate than is predicted from QNM theory (see above, Sec. IV B). Motivated by the results of Sec. IV B, notably by the fact that a superposition of three QNMs can fit very well the NR waveforms starting from the peak of the energy flux, we choose the peak of the energy flux as the best matching point.

Having shown a reasonably close match for each of the radiative multipoles between the effective Newtonian model and the numerical data, it stands to reason that the total recoil calculated with this model should agree as well. This is shown in Fig. 8, where we have also varied the matching point around t_{peak} . We first note the close agreement between the eN models with varying t_{match} , suggesting the inspiral-to-ringdown matching method described above is relatively robust. Not surprisingly, since the individual modes agree, we also find reasonable agreement between the NR data and the eN predictions for the recoil.

However, this agreement may be partially fortuitous, since the eN model cannot predict the mode phase shifts around $t = t_{\text{peak}}$, most notably that of the I^{44} mode described above. In Sec. VI B below, we will examine this phasing in greater detail and show how it affects the overall kick. At this point, we unfortunately do not have a clear understanding of the underlying cause of the phase shift, but it may well be related to the slightly different times of transition from inspiral to ringdown for the different modes. Preliminary results also suggest that this dephasing effect is reduced in more extreme mass-ratio systems, as we shall see in the Appendix.

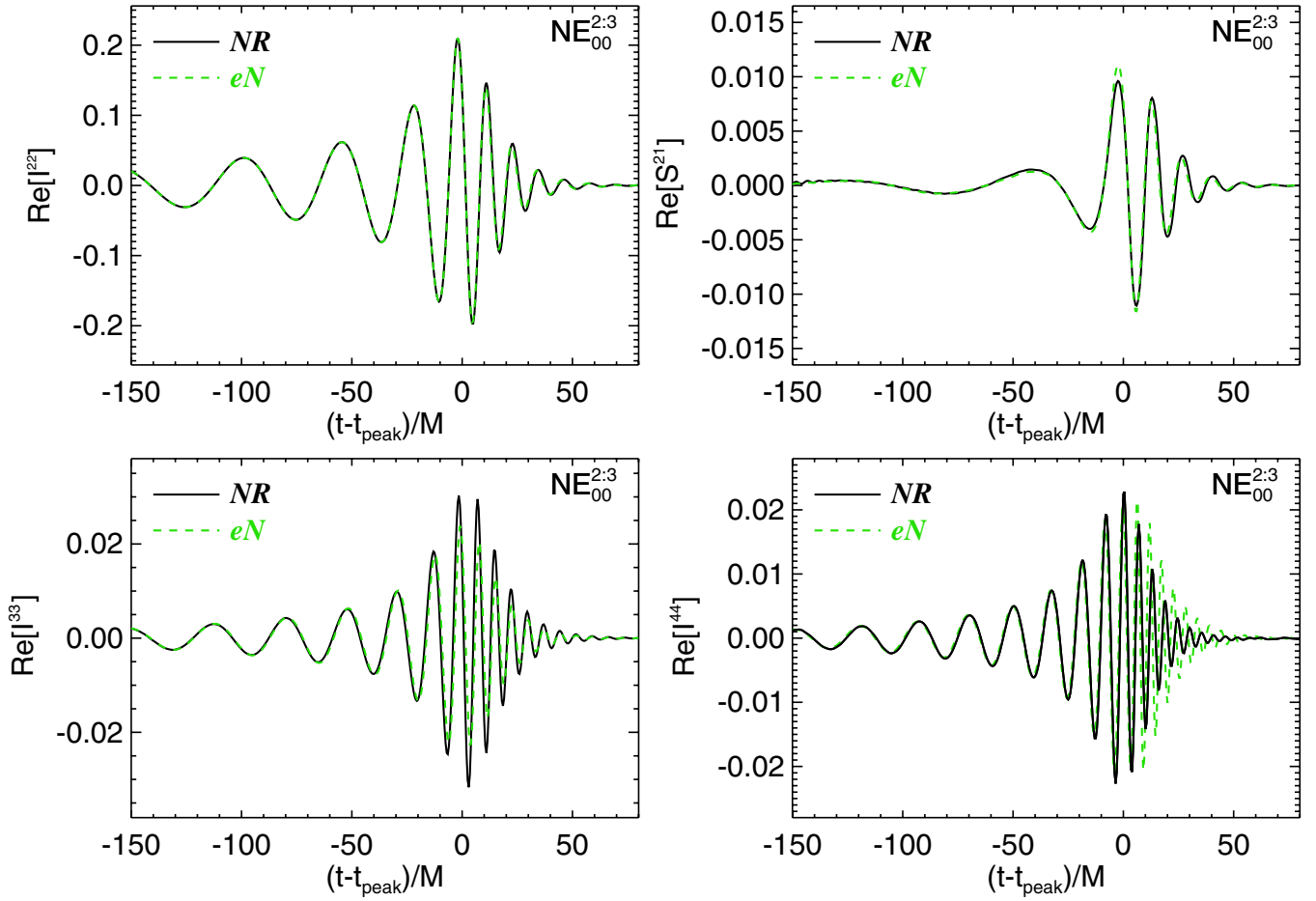


FIG. 7 (color online). Comparison of the effective Newtonian and NR radiative modes during inspiral, merger, and RD phases. The data refer to the $NE_{00}^{1:2}$ run. We denote with t_{peak} the time at which l^{22} reaches its maximum.

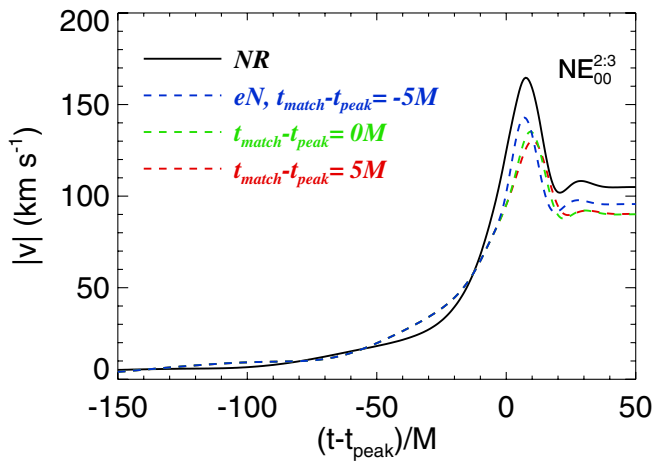


FIG. 8 (color online). Comparison of the effective Newtonian model and NR predictions for the recoil velocity for a range of inspiral-RD matching points. We denote with t_{peak} the time at which l^{22} reaches its maximum. The data refer to the $NE_{00}^{2:3}$ run.

VI. ANATOMY OF THE KICK

In the above sections, we have laid the groundwork for a multipolar analysis of the gravitational recoil, describing the momentum flux as a combination of radiative multipole modes. Along with the pseudoanalytic models for the inspiral and ringdown phases, we can now give a detailed description of the “anatomy” of the kick, namely, the way the different modes combine to produce a peak recoil velocity, followed by a characteristic antikick and then asymptotic approach to the final value of the BH recoil.

A. Contribution from different moments

In Sec. III A, we showed how the radiative multipole moments contribute to the linear-momentum flux through the integral of the Ψ_4 scalar [Eqs. (10) and (12)]. Here, we want to determine exactly which modes we need to include in the multipole expansion Eq. (13) to get a good representation of the full recoil, and which are the pairs of modes in Eq. (21) that contribute most.

By including only a select choice of terms in the ψ_4 expansion Eq. (10), we can calculate the linear-momentum

flux by direct integration of Eq. (12) and compare it with the predictions of Eqs. (17)–(21), in each case including only the appropriate moments. This is a good way of double-checking those lengthy equations term by term, and in practice we find excellent agreement, limited only by the numerical accuracy of the simulations. Similarly, we can use this method of truncated expansion to determine which modes are necessary for calculating the recoil up to a given accuracy. The results of using higher and higher order multipolar moments are shown in Figs. 9 and 10 for the $\text{NE}_{00}^{2:3}$ and $\text{NE}_{00}^{1:2}$ runs, respectively.

In the left panels of Figs. 9 and 10 we show with a solid curve the exact recoil velocity from Eq. (12), with a dashed curve the contribution from terms up to $\ell = 4$, i.e., those obtained from Eqs. (17)–(19), and with a dotted curve the contribution from just the three leading terms in Eq. (21), valid for nonprecessing BHs with kicks in the orbital plane. We conclude that the linear-momentum flux is dominated by the $I^{33}I^{22*}$, $I^{33}I^{44*}$, and $S^{21}I^{22*}$ terms, which combine to produce the primary kick and antick agreeing with the exact result within $\lesssim 10\%$ throughout the entire merger. Note that the flux from the $S^{32}I^{33*}$ term, while not insignificant in Fig. 4, contributes almost nothing to the net recoil velocity. This is largely due to phase relations between the various modes during the transition from inspiral to ringdown, described below in Sec. VIB.

In the right panels of Figs. 9 and 10 we show the difference between the calculation obtained including terms up to $\ell = 3, 4, 5, 6$, and the exact result. It seems clear that we need modes up to and including $\ell = 4$ to get an accurate estimate of the recoil velocity. For more extreme mass ratios, higher-order moments become relatively more important, but remain strongly subdominant to the $\ell \leq 4$ modes [11,71].

To understand more clearly the relative contributions of the different modes to the total recoil, we will include an analysis of a few more simulations including nonprecessing spins. As mentioned above in Sec. III A, nonprecessing spins do not introduce any additional moments compared to the nonspinning simulations, but simply modify the relative amplitudes of the different modes in Eq. (21) by adding the spin terms. Thus, once we determine how the spins modify the individual modes, we can use the same analysis for the spinning and nonspinning cases.

Again equating the radiative multipole moments with the source moments, we get the leading-order spin-orbit modifications to Eqs. (37a)–(37g) [see Eqs. (3.14), (3.20) in Ref. [41] and Eq. (5.5) in Ref. [78]]:

$$S_{\text{SO}}^{21} = -4i\sqrt{\frac{2\pi}{5}}\eta R\omega^3 e^{-i\phi}\Delta^z, \quad (45a)$$

$$I_{\text{SO}}^{22} = \frac{64}{3}i\sqrt{\frac{2\pi}{5}}\eta R^2\omega^4 e^{-2i\phi}\xi^z, \quad (45b)$$

$$S_{\text{SO}}^{32} = -\frac{32}{3}\sqrt{\frac{2\pi}{7}}\eta R^2\omega^4 e^{-2i\phi}\xi^z, \quad (45c)$$

$$I_{\text{SO}}^{31} = -\frac{2}{3}\sqrt{\frac{\pi}{35}}\eta R^3\omega^5 e^{-i\phi}\Sigma_{31}^z, \quad (45d)$$

$$I_{\text{SO}}^{33} = 54\sqrt{\frac{\pi}{21}}\eta R^3\omega^5 e^{-3i\phi}\Sigma_{33}^z, \quad (45e)$$

where we have introduced the spin vectors

$$\Sigma_{31} \equiv \frac{11}{2}\frac{\delta m}{M}\mathbf{S} + \frac{1}{2}(11 - 39\eta)\mathbf{\Delta}, \quad (46a)$$

$$\Sigma_{33} \equiv \frac{3}{2}\frac{\delta m}{M}\mathbf{S} + \frac{3}{2}(1 - 5\eta)\mathbf{\Delta}. \quad (46b)$$

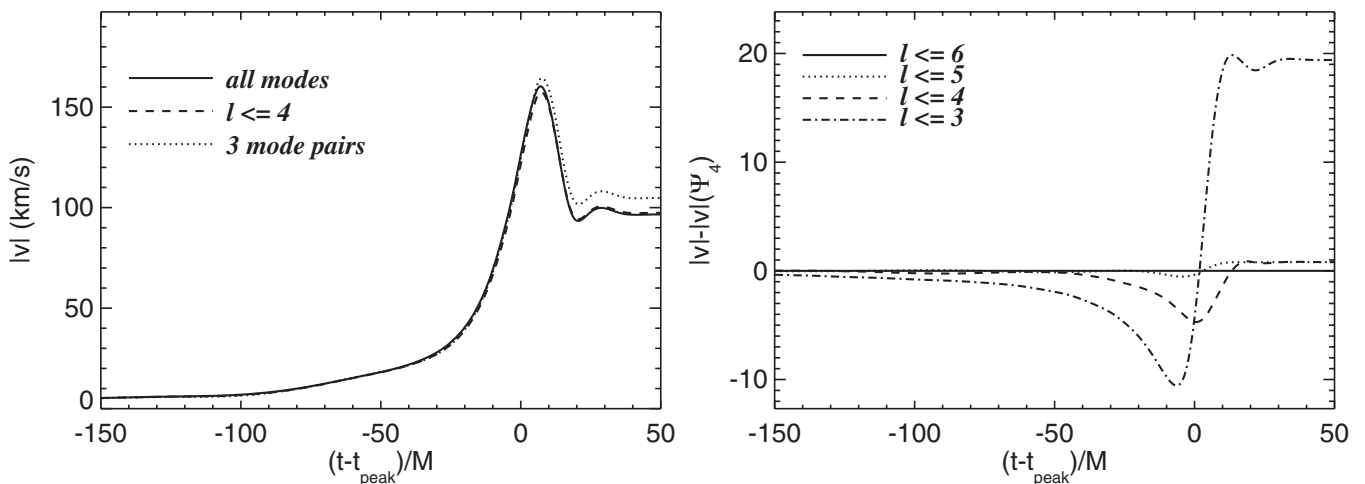
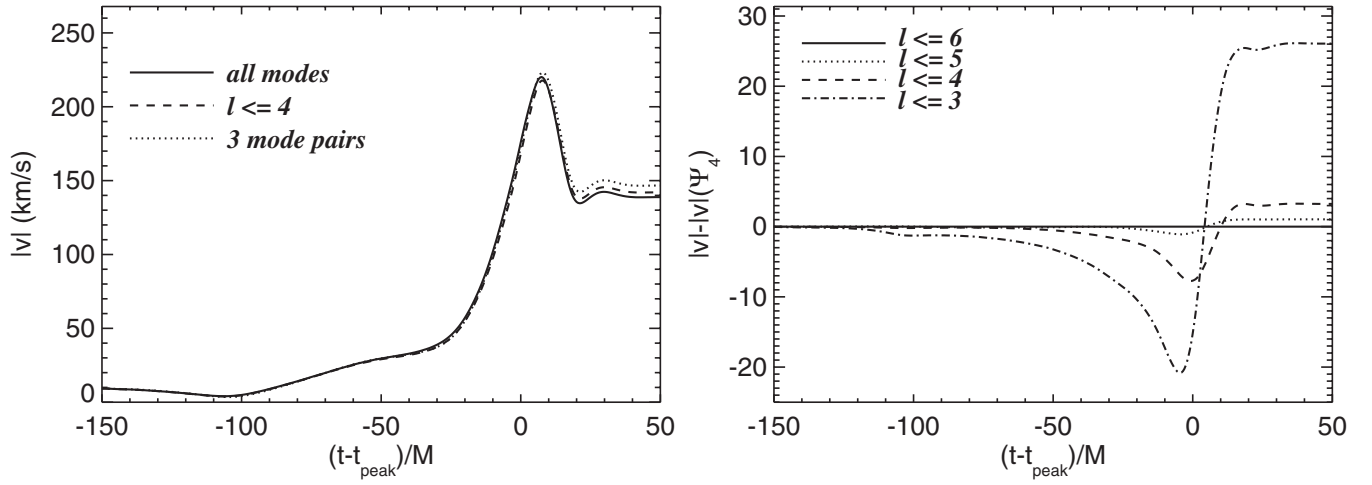


FIG. 9. In the left panel we show the net recoil kick, integrated from the linear-momentum flux via Eq. (12) (solid curve), from all modes with $\ell \leq 4$ (dashed curve), and just the first three terms in Eq. (21) (dotted curve). In the right panel we show the difference between the exact result and the Ψ_4 expansion Eq. (10), limited to $\ell \leq 3, 4, 5, 6$. The data refer to the $\text{NE}_{00}^{2:3}$ run. We denote with t_{peak} the time at which I^{22} reaches its maximum.

FIG. 10. Same as Fig. 9, but for the $\text{NE}_{00}^{1:2}$ run.

In all of the simulations considered here, the dimensionless spins are equal ($|a_1|/m_1 = |a_2|/m_2$) and point in opposite directions, $\xi^z = 0$, so for the leading-order terms in Eq. (21) we are left only with the modifications of S^{21} and I^{33} , due to Δ^z and Σ_{33}^z , respectively. Then Eqs. (37) and (45) give the linear-momentum flux during the inspiral for each of the first three dominant terms in Eq. (21):

$$F_{\text{insp}}^{21,22} = \frac{16}{45} i \frac{\mu^2}{M} R^3 \omega^6 (2\delta m R^2 \omega + 3\Delta^z) e^{i\phi}, \quad (47a)$$

$$F_{\text{insp}}^{22,33} = -\frac{36}{7} i \frac{\mu^2}{M} R^5 \omega^7 (\delta m + \omega \Sigma_{33}^z) e^{i\phi}, \quad (47b)$$

$$F_{\text{insp}}^{33,44} = -\frac{64}{7} i \frac{\mu^2}{M} (1 - 3\eta) R^7 \omega^9 (\delta m + \omega \Sigma_{33}^z) e^{i\phi}. \quad (47c)$$

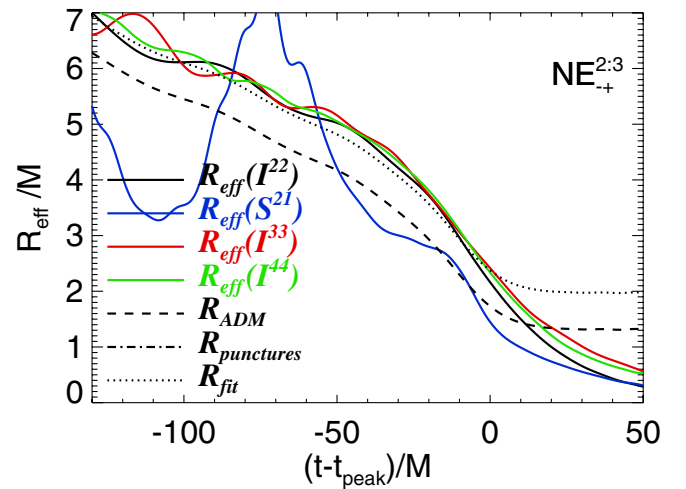
While these flux formulas contain terms of various orders in ω , we expect that the effective Newtonian scaling of R ensures that we are including all relevant PN terms, at least in the cases where the δm terms dominate over the spin corrections. When the spin terms begin to dominate, we find that it becomes more difficult to use a single effective R for all modes. This can be seen in Fig. 11, which plots R_{eff} as in Fig. 6, but for the $\text{NE}_{00}^{2:3}$ run, where the Δ^z and δm terms in Eq. (47a) are comparable, making it difficult to derive a reasonable $R_{\text{eff}}(S^{21})$.

Even for nonspinning runs, in order to get reasonable agreement with the NR data, we find that one must be careful towards the end of the inspiral to distinguish between $\omega_D^{I^{22}}$ and $\omega_D^{S^{21}}$ in Eq. (47a):

$$F_{\text{insp}}^{21,22} \propto (\mu^2/M) R^3 (\omega_D^{I^{22}})^3 (\omega_D^{S^{21}})^3 (2\delta m R^2 \omega_D^{S^{21}} + 3\Delta^z). \quad (48)$$

The amplitudes of these fluxes are plotted in Fig. 12 for the four runs $\text{NE}_{-+}^{2:3}$, $\text{NE}_{+-}^{2:3}$, $\text{NE}_{00}^{2:3}$, and EQ_{+-} . As seen in Table I, the $\text{NE}_{-+}^{2:3}$ run has $\Delta^z = 0.2M^2$, while the $\text{NE}_{+-}^{2:3}$ run has $\Delta^z = -0.2M^2$, respectively, adding destructively and constructively with the δm term in Eq. (47a). This

difference is clearly seen in the blue curves in the top two panels of Fig. 12. Also notable in these plots is the somewhat smaller difference in the amplitudes of $F^{22,33}$, due to a similar effect from the constructive/destructive additions of δm and Σ_{33}^z in Eq. (47b). As we see in Fig. 12, $\text{NE}_{00}^{2:3}$ appears to be the average of $\text{NE}_{+-}^{2:3}$ and $\text{NE}_{-+}^{2:3}$, while the flux from EQ_{+-} is strongly suppressed due to the $\delta m = 0$ terms in Eq. (47), leaving only the flux from the terms proportional to $\Delta^z = -0.2M^2$ and $\Sigma_{33}^z = 0.075$. However, as noted above, when the spin terms dominate the flux, as in the case of equal-mass BHs, the eN model with a single R_{eff} begins to break down. Yet, even in this situation, Eqs. (47a)–(47c) still have a qualitative (if not quantitative) predictive value, including the relative phases between the different mode-pair fluxes during the inspiral.

FIG. 11 (color online). R_{eff} derived from different multipole modes, as in Fig. 6, for the $\text{NE}_{+-}^{2:3}$ run. The S^{21} mode for this run has comparable contributions from δm and Δ^z , making it difficult to derive a reasonable $R_{\text{eff}}(S^{21})$.

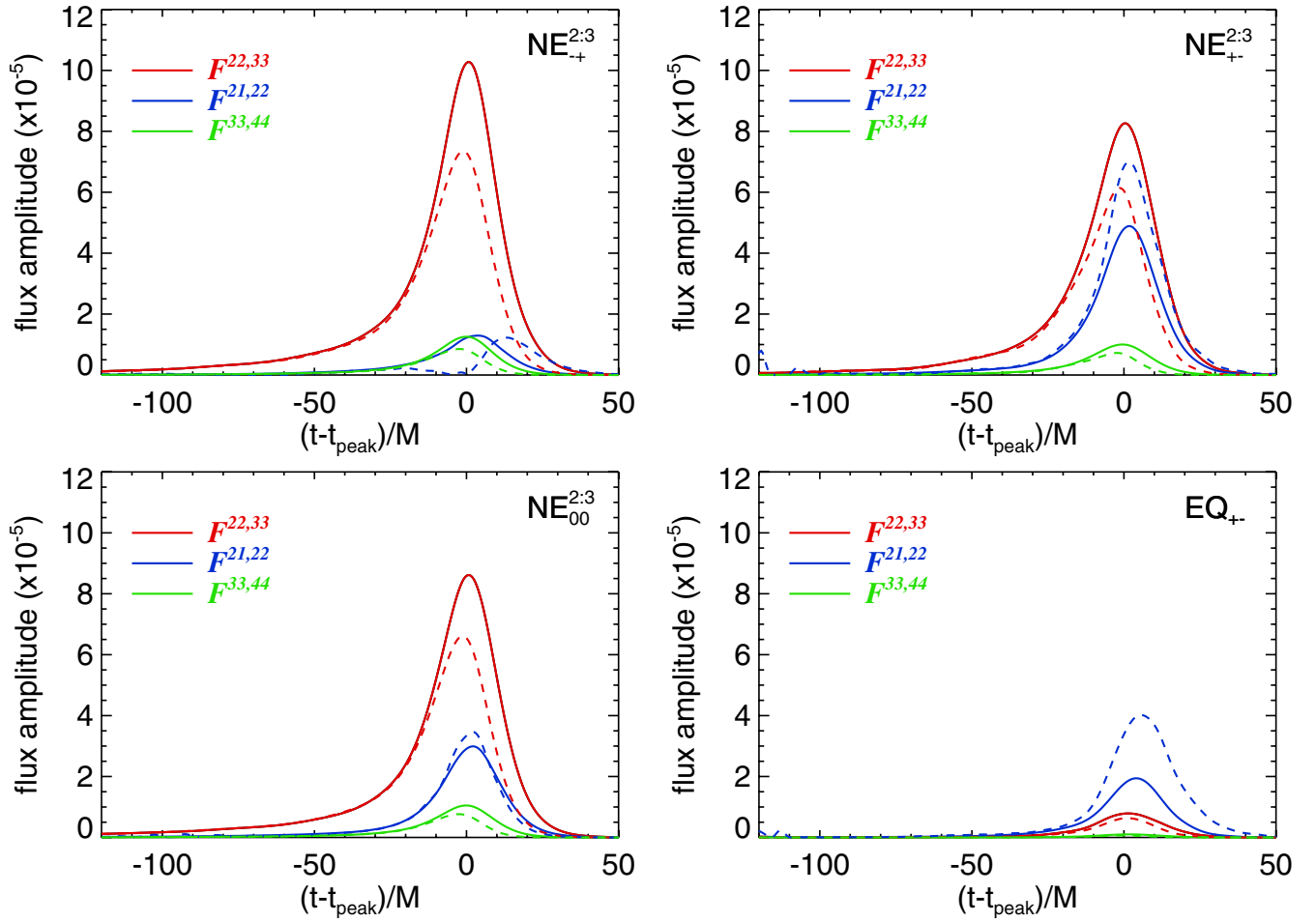


FIG. 12 (color online). Relative amplitudes of the dominant multipole mode pairs in the linear-momentum flux. Also shown as the dashed curves are the eN model predictions for the flux amplitudes. We denote with t_{peak} the time at which I^{22} reaches its maximum.

In each panel of Fig. 12, we also plot with dashed lines the eN prediction for the various flux amplitudes. In almost all cases, the eN flux is quite close to the NR results up to about $10M$ before t_{peak} , when the eN model begins to break down, especially for the spinning runs. The amplitude differences near the peaks are comparable to those seen in Fig. 7 for the $\text{NE}_{00}^{2:3}$ run. The notable exception is the $F^{21,22}$ flux from the $\text{NE}_{+}^{2:3}$ and EQ_{+-} runs, where the spin terms dominate over the δm terms.

B. Transition to ringdown and the dephasing of the multipole modes

Since the flux vectors defined by Eq. (47) will not generally be collinear, to understand the time evolution of the recoil velocity, we must first understand the phase relations between the different modes. From Eqs. (37), (45), and (47), we see that, during the inspiral phase, the individual moments and the resulting flux vectors evolve according to a single orbital phase ϕ , with $F_{\text{insp}}^{21,22}$ pointing in the opposite direction to $F_{\text{insp}}^{22,33}$ and $F_{\text{insp}}^{33,44}$. However, as we can see from Fig. 2, as the binary evolves from inspiral

to RD, the frequency (and thus phase) of the S^{21} mode decouples from the other dominant modes. Upon closer inspection, we find that even the I^{22} , I^{33} , and I^{44} modes deviate from each other enough to undergo a significant phase shift at the inspiral-RD transition.

To quantify these effects, we define the following phase differences:

$$\cos\psi^{2-3} = \hat{\mathbf{F}}_{\text{insp}}^{21,22} \cdot \hat{\mathbf{F}}_{\text{insp}}^{22,33}, \quad (49a)$$

$$\cos\psi^{2-4} = \hat{\mathbf{F}}_{\text{insp}}^{21,22} \cdot \hat{\mathbf{F}}_{\text{insp}}^{33,44}, \quad (49b)$$

$$\cos\psi^{3-4} = \hat{\mathbf{F}}_{\text{insp}}^{22,33} \cdot \hat{\mathbf{F}}_{\text{insp}}^{33,44}. \quad (49c)$$

Here we use the notation $\psi^{m-m'}$ to describe the phase difference between two complex flux vectors, where m and m' correspond to the *larger* m values of each mode pair that makes up the flux. These definitions are valid throughout the inspiral, merger, and ringdown phases. In the inspiral phase, we can see that, for the unequal-mass runs where δm dominates with respect to the spin terms in Eqs. (47a)–(47c), we have

$$\cos\psi_{\text{insp}}^{2-3} = \cos\psi_{\text{insp}}^{2-4} = -1, \quad \cos\psi_{\text{insp}}^{3-4} = 1. \quad (50)$$

For the EQ₊₋ run with $\delta m = 0$, Eq. (47) predicts that all phases have $\cos\psi_{\text{insp}} = 1$ during the inspiral [as shown in Table I, Δ^z and Σ_{33}^z have opposite signs, so all the flux vectors in Eq. (47) are parallel]. During the RD phase, using Eq. (42), we can approximate the flux vectors and phase evolution in terms of the fundamental QNM frequencies $\sigma_{\ell m 0}$:

$$F_{\text{RD}}^{21,22} \simeq F_{\text{match}}^{21,22} \exp[-i(\sigma_{210} - \sigma_{220}^*)(t - t_{\text{match}})], \quad (51a)$$

$$F_{\text{RD}}^{22,33} \simeq F_{\text{match}}^{22,33} \exp[-i(\sigma_{220} - \sigma_{330}^*)(t - t_{\text{match}})], \quad (51b)$$

$$F_{\text{RD}}^{33,44} \simeq F_{\text{match}}^{33,44} \exp[-i(\sigma_{330} - \sigma_{440}^*)(t - t_{\text{match}})], \quad (51c)$$

where the $F_{\text{match}}^{\ell m, \ell' m'}$ fluxes include complex phase information at the matching point. Taking the phase differences between these RD modes gives

$$\cos\psi_{\text{RD}}^{2-3} \simeq \cos[(\omega_{210} - 2\omega_{220} + \omega_{330})(t - t_{\text{match}}) + \Phi_{\text{match}}^{2-3}], \quad (52a)$$

$$\cos\psi_{\text{RD}}^{2-4} \simeq \cos[(\omega_{210} - \omega_{220} - \omega_{330} + \omega_{440}) \times (t - t_{\text{match}}) + \Phi_{\text{match}}^{2-4}], \quad (52b)$$

$$\cos\psi_{\text{RD}}^{3-4} \simeq \cos[(\omega_{220} - 2\omega_{330} + \omega_{440})(t - t_{\text{match}}) + \Phi_{\text{match}}^{3-4}]. \quad (52c)$$

Here Φ_{match} is a phase offset determined at the transition from inspiral to ringdown. Quite interestingly, we find that for the range of final BH spin parameters $0.5 \leq a_f/M_f \leq 0.8$, the linear combinations of frequencies in Eqs. (52a)–(52c) vary by less than $\sim 5\%$. Thus, if we compute the above expressions for the $\omega_{\ell m 0}$ corresponding to $a_f/M_f = 0.7$, we have [75]

$$\cos\psi_{\text{RD}}^{2-3} \simeq \cos\left[\frac{0.23}{M_f}(t - t_{\text{match}}) + \Phi_{\text{match}}^{2-3}\right], \quad (53a)$$

$$\cos\psi_{\text{RD}}^{2-4} \simeq \cos\left[\frac{0.22}{M_f}(t - t_{\text{match}}) + \Phi_{\text{match}}^{2-4}\right], \quad (53b)$$

$$\cos\psi_{\text{RD}}^{3-4} \simeq \cos\left[\frac{0.012}{M_f}(t - t_{\text{match}}) + \Phi_{\text{match}}^{3-4}\right]. \quad (53c)$$

Even more intriguing, we find that for the unequal-mass simulations described above, the phase relations during the inspiral and RD are almost identical, regardless of spin orientations. This can be seen clearly in Fig. 13, which plots $\cos\psi$ during inspiral, merger, and RD for the different runs. The collinearity of the flux vectors is clear during the

inspiral phase, and the sinusoidal oscillations of the phases during RD agree well with the analytic predictions (plotted in dashed curves in Fig. 13). Since the analytic models are most reliable during the inspiral and RD phases (but have more difficulty tracing the merger portion), we omit in Fig. 13 the transition region of $-10M \leq (t - t_{\text{peak}}) \leq 10M$. The analytic phase relations during inspiral are determined by Eq. (50) and during ringdown by Eqs. (53a)–(53c). Here we use a t_{match} (and corresponding Φ_{match}) about $20M$ after t_{peak} to ensure that the multipole moments are truly dominated by the fundamental QNMs, and thus Eqs. (53a)–(53c) are valid. Note that the phase differences for EQ₊₋ are particularly noisy since the amplitude of the F^{33} moment is zero to leading order, and thus it is more difficult to extract a clear phase for that mode.

The feature that is most difficult to explain from an analytic model alone (and is thus omitted from the eN curves in Fig. 13) is the roughly 180-degree jump in phase between $F_{\text{insp}}^{22,33}$ and $F_{\text{insp}}^{33,44}$, beginning around $20M$ before the peak. This appears to be a feature in all the unequal-mass runs examined, but preliminary results suggest that is less significant (i.e., a smaller phase shift) for more extreme mass-ratio systems, as we shall discuss in the Appendix. We are not able to explain it with the additional RD overtone modes described in Sec. VB, but using slightly different RD matching points for the different multipoles may help explain the issue.

C. The antikick

These flux amplitudes and phase relations can now be used to understand the amplitude of the kick and antikick, by which we mean the difference between the peak and the final recoil velocities (see Fig. 1 for an example). Throughout the inspiral phase, the amplitude and rotational frequency of the flux vectors in Eq. (47) are monotonically increasing, giving the familiar outward-spiraling trajectory for the velocity vector. Then, in the RD phase, the dominant frequencies are nearly constant while the amplitudes decay exponentially for each mode, giving an inward spiral that decays like a damped harmonic oscillator around the final asymptotic recoil velocity.

These trajectories in velocity space can be seen in Fig. 14, along with the instantaneous flux vectors from the competing mode pairs. Clearly, even small changes in the mass ratios and spins orientations of the BHs can give a rather diverse selection of velocity trajectories. Note, in particular, the difference between the NE₊₋^{2:3} run, dominated by the $F^{22,33}$ flux and a large antikick, and the EQ₊₋ run, which in contrast is dominated by the $F^{21,22}$ flux. We find that the EQ₊₋ run has *no* antikick, which can be explained by the slowly rotating flux vector that does not spiral back inwards, but rather drifts off slowly towards infinity during the ringdown. The difference between these two runs can be explained entirely by examining the real part of their fundamental QNM frequencies $\sigma_{\ell m 0}$, which in

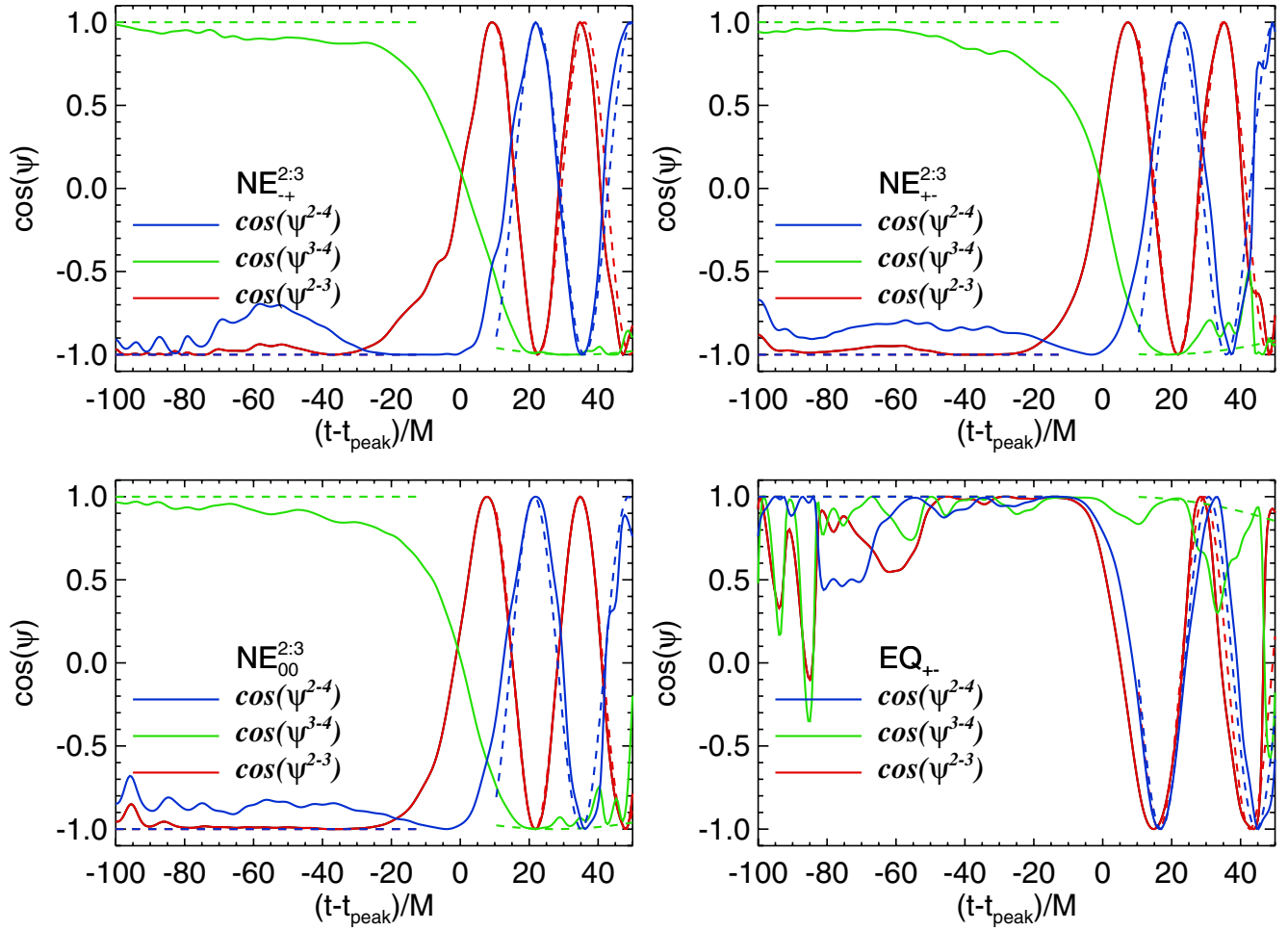


FIG. 13 (color online). Phase differences between different mode-pair flux vectors, as defined by Eqs. (49a)–(49c). The data refer to the $NE_{+-}^{2:3}$ (upper left panel), $NE_{-+}^{2:3}$ (upper right panel), $NE_{00}^{2:3}$ (lower left panel), and EQ_{+-} (lower right panel) runs. The dashed curves are the eN model predictions of Eqs. (50) and (53). We denote with t_{peak} the time at which I^{22} reaches its maximum.

turn determine the rotation rates of the flux vectors in Eq. (51): EQ_{+-} is dominated by $\omega_{220} - \omega_{210} = 0.08/M_f$, a much slower frequency than $\omega_{330} - \omega_{220} = 0.31/M_f$, which causes the rapid inward spiral of the $NE_{-+}^{2:3}$ run.

To calculate the recoil velocity, we must integrate the linear-momentum flux vectors in time. (For the initial velocity vector, we integrate the post-Newtonian approximation for the momentum flux from $t = -\infty$ to the beginning of the numerical simulation [43]. This effectively sets the centers of the spiral curves in Fig. 14 to correspond to the origin in velocity space.) We can get a reasonable analytic approximation by using Eqs. (47) and (51) for the inspiral and RD phases, respectively. In the adiabatic inspiral, the complex recoil velocity $v = v_x + iv_y$ can be written as

$$v_{\text{insp}} = \int_{-\infty}^{t_{\text{match}}} F(t') dt' \simeq \frac{1}{i\omega_{\text{match}}} F_{\text{match}}, \quad (54)$$

while for the RD portion we have

$$v_{\text{RD}}(t) = \int_{t_{\text{match}}}^t F(t') dt' \simeq \sum_{\ell m, \ell' m'} \frac{i F_{\text{match}}^{\ell m, \ell' m'}}{\sigma_{\ell m 0} - \sigma_{\ell' m' 0}^*} [e^{-i(\sigma_{\ell m 0} - \sigma_{\ell' m' 0}^*)(t - t_{\text{match}})} - 1], \quad (55a)$$

$$v_f \equiv v_{\text{RD}}(t \rightarrow \infty) \simeq \sum_{\ell m, \ell' m'} \frac{-i}{\sigma_{\ell m 0} - \sigma_{\ell' m' 0}^*} F_{\text{match}}^{\ell m, \ell' m'}, \quad (55b)$$

summing the contributions from each pair of modes

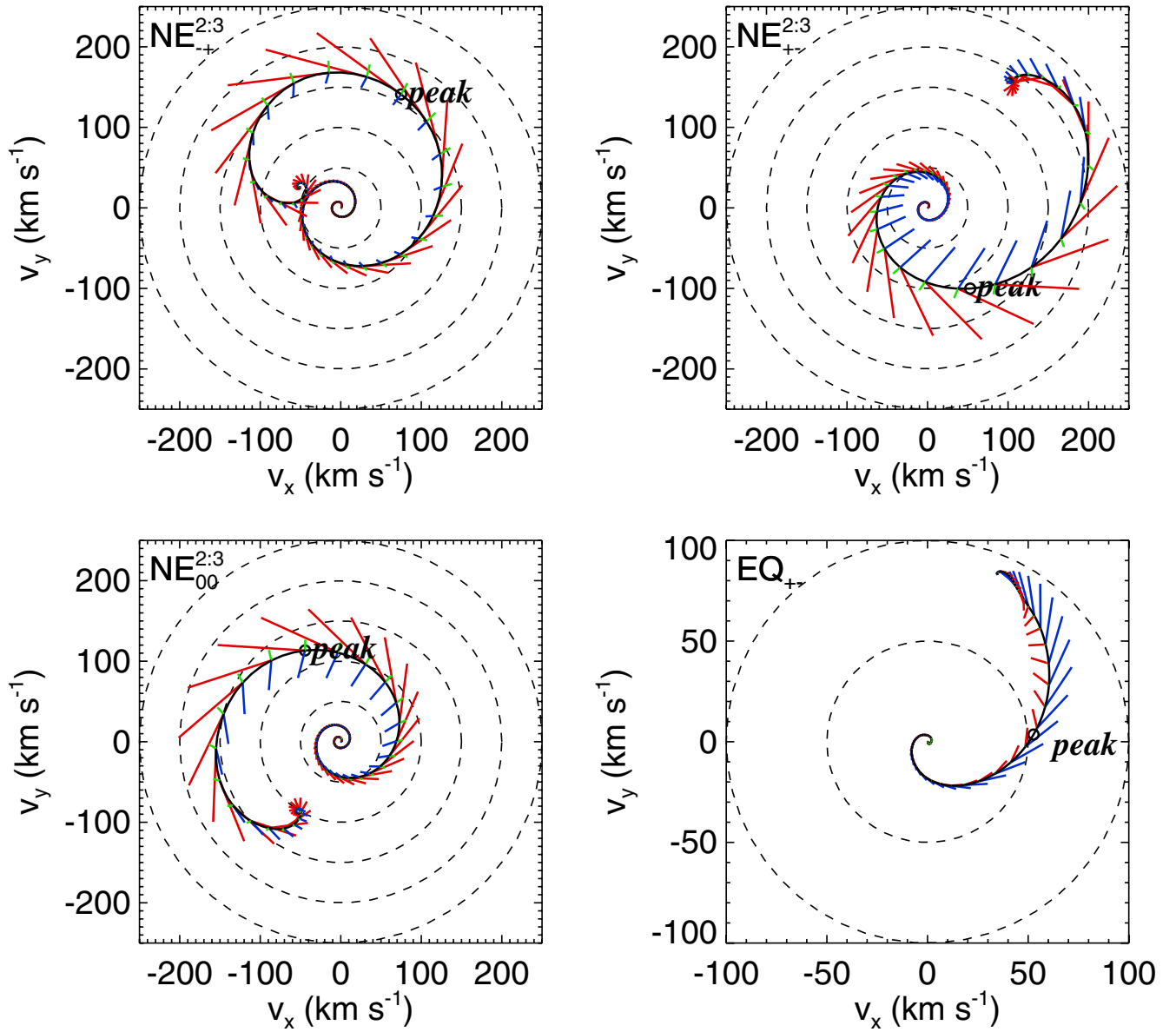


FIG. 14 (color online). The recoil velocity vector evolving in the v_x - v_y plane (black solid curve), along with the flux vectors due to the three mode pairs at each time interval along the velocity trajectory (same color scheme as Fig. 12). The data refer to the $NE_{+}^{2:3}$ (upper left panel), $NE_{-}^{2:3}$ (upper right panel), $NE_{00}^{2:3}$ (lower left panel), and EQ_{+-} (lower right panel) runs. We denote with the label *peak* the time at which I^{22} reaches its maximum.

($\ell m, \ell' m'$). Then the total velocity in each of the dominant mode pairs is given by

$$\int F^{21,22}(t') dt' = \frac{16}{45} \frac{\mu^2}{M} R_{\text{match}}^3 \omega_{\text{match}}^5 (2\delta m R_{\text{match}}^2 \omega_{\text{match}} + 3\Delta^z) \left[1 - \frac{i\omega_{\text{match}} e^{i\phi_{\text{match}}^{21,22}}}{\sigma_{210} - \sigma_{220}^*} \right], \quad (56a)$$

$$\int F^{22,33}(t') dt' = -\frac{36}{7} \frac{\mu^2}{M} R_{\text{match}}^5 \omega_{\text{match}}^6 (\delta m + \omega_{\text{match}} \Sigma_{33}^z) \left[1 - \frac{i\omega_{\text{match}} e^{i\phi_{\text{match}}^{22,33}}}{\sigma_{220} - \sigma_{330}^*} \right], \quad (56b)$$

$$\int F^{33,44}(t') dt' = -\frac{64}{7} \frac{\mu^2}{M} (1 - 3\eta) R_{\text{match}}^7 \omega_{\text{match}}^8 (\delta m + \omega_{\text{match}} \Sigma_{33}^z) \left[1 - \frac{i\omega_{\text{match}} e^{i\phi_{\text{match}}^{33,44}}}{\sigma_{330} - \sigma_{440}^*} \right]. \quad (56c)$$

The phase $\phi_{\text{match}}^{21,22}$ is defined as the angle made between the flux vector $F^{21,22}$ and the velocity vector \mathbf{v} at the beginning of the ringdown (with other phases $\phi_{\text{match}}^{22,33}$, $\phi_{\text{match}}^{33,44}$ defined analogously). Because of the anomalous phase shifts and departure

from adiabaticity at the transition from inspiral to ring-down, these angles are difficult to predict with an independent analytic model, but can be calculated easily from plots like Fig. 14. However, the accuracy of Eq. (56) is limited by the adiabaticity condition of Eq. (54) as well as the accuracy of the spin-orbit corrections to the eN model (see Fig. 11). Therefore, in analyzing the antikick in terms of RD modes, we find it more useful simply to integrate Eq. (54) directly from the numerical data during the inspiral, and then attach the fundamental QNM terms from Eq. (55) at the matching point $t_{\text{match}} = t_{\text{peak}}$.

Given v_{match} at the end of the inspiral, we can use this quasianalytic approach to predict the maximum and final recoil velocities (v_{max} and v_f , respectively). These predictions are plotted as black dashed curves in Fig. 15, to be compared with the solid black curves of the exact NR results. Within this context, we define the antikick magnitude as

$$f_{\text{ak}} \equiv \frac{v_f - v_{\text{max}}}{v_{\text{max}}} \quad (57)$$

and the net ringdown contribution as

$$f_{\text{RD}} \equiv \frac{v_f - v_{\text{match}}}{v_{\text{match}}}, \quad (58)$$

where v_{max} and v_f are the (real-valued) velocity magnitudes calculated analytically from Eq. (55).

In the case of the $\text{NE}_{+}^{2:3}$ run, where the recoil is almost entirely dominated by the $F^{22,33}$ flux, we find a large antikick with $f_{\text{ak}} = -0.53$ and $f_{\text{RD}} = -0.5$. On the other hand, for the $\text{NE}_{+-}^{2:3}$ run, as can be seen in Fig. 15, the net recoil velocity continues to increase after $t_{\text{match}} = t_{\text{peak}}$ before turning around for a small antikick of $f_{\text{ak}} = -0.11$. The total effect of the ringdown phase is actually to increase the recoil with $f_{\text{RD}} = 0.68$. An intermediate effect is seen for the $\text{NE}_{00}^{2:3}$ run, with $f_{\text{ak}} = -0.28$ and

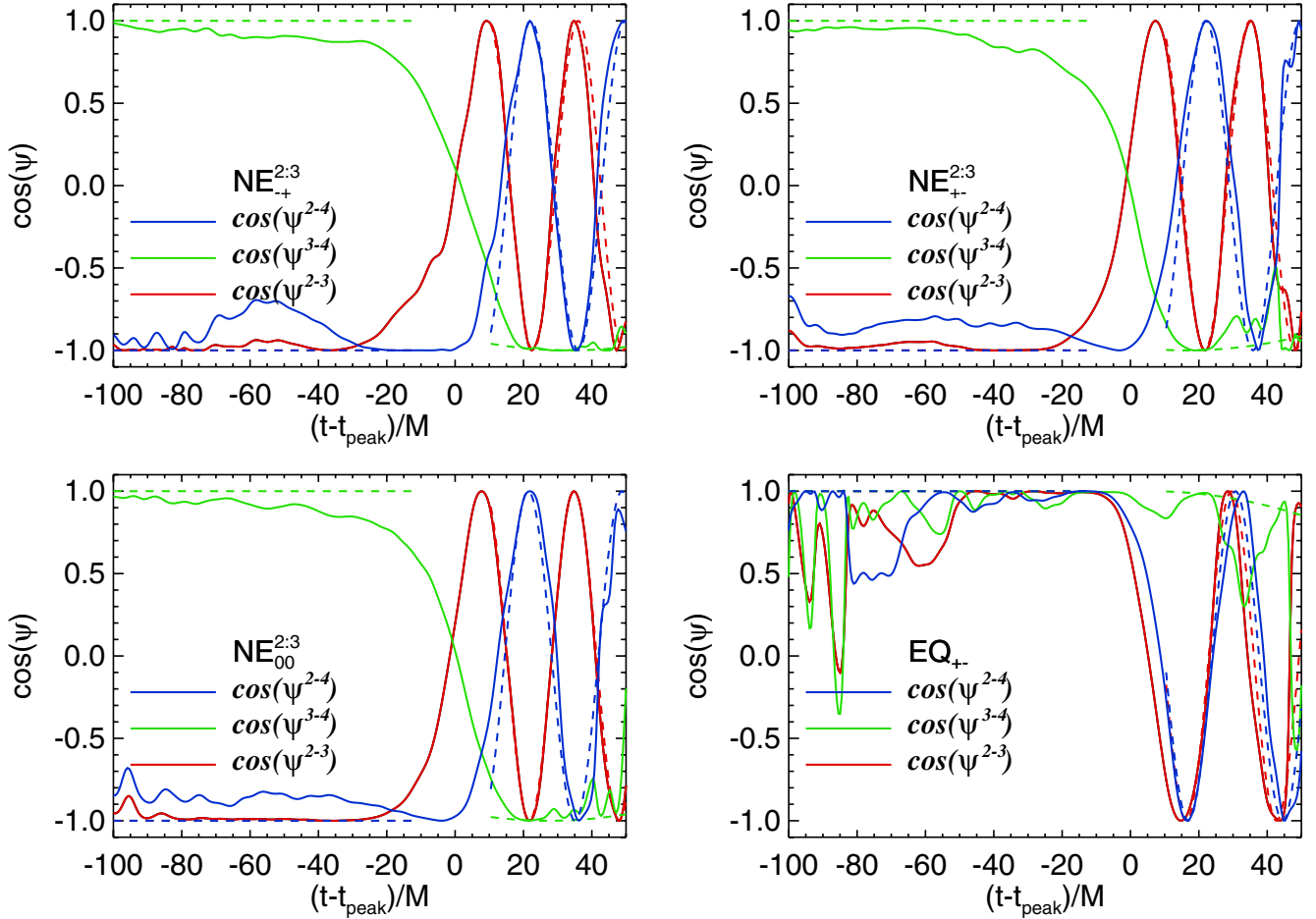


FIG. 15 (color online). Relative contributions to the total recoil velocity from the different multipole mode pairs. $I^{22}I^{33*}$ (red curve) is the dominant mode for unequal-mass binary systems, while $S^{21}I^{22*}$ (blue curve) dominates for spinning, equal-mass binary systems. Also plotted is the contribution from the $S^{32}I^{33*}$ flux terms (blue dashed curve), demonstrating its very small contribution to the total recoil velocity. For $t > t_{\text{match}} = t_{\text{peak}}$, we include the quasianalytic prediction for $v_{\text{RD}}(t)$ (black dashed curves), based on the fundamental RD modes from Eq. (55). The data refer to the $\text{NE}_{+}^{2:3}$ (upper left panel), $\text{NE}_{+-}^{2:3}$ (upper right panel), $\text{NE}_{00}^{2:3}$ (lower left panel), and EQ_{+-} (lower right panel) runs. We denote with t_{peak} the time at which I^{22} reaches its maximum.

$f_{\text{RD}} = -0.04$. However, as seen above in Fig. 14, for the EQ_{+-} run, we see no antikick, with $f_{\text{ak}} = -0.01$ and $f_{\text{RD}} = 0.58$.

In general, we find the magnitude of the antikick is primarily dependent on the relative magnitudes of the S^{21} and I^{33} moments. When S^{21} dominates (e.g., when δm and Δ^z add constructively), the ringdown rotation is slow and there is a small antikick, whereas a dominant I^{33} mode (e.g., large δm or no spins) gives a rapidly rotating ringdown flux and thus a large antikick. Furthermore, from Eq. (47), we see that for nonspinning BHs, both the S^{21} and I^{33} modes share the same mass and frequency scaling, so the relative size of the antikick should be roughly independent of the mass ratio (see the Appendix for a caveat).

We would like a more quantitative picture of how these flux vectors add constructively and destructively to give the total recoil velocity to support the analytic estimates presented above. Using $\mathbf{v} = \int \mathbf{F} dt$, we can write

$$\frac{d}{dt}|\mathbf{v}| = \frac{d}{dt}(\hat{\mathbf{v}} \cdot \mathbf{v}) = \hat{\mathbf{v}} \cdot \mathbf{F}, \quad (59)$$

where $\hat{\mathbf{v}} \cdot \hat{\mathbf{v}} = 1$. Breaking \mathbf{F} up into the contributions of the dominant modes as above, and then integrating in time gives

$$\mathbf{v}^{21,22} = \int \hat{\mathbf{v}} \cdot \mathbf{F}^{21,22} dt, \quad (60a)$$

$$\mathbf{v}^{22,33} = \int \hat{\mathbf{v}} \cdot \mathbf{F}^{22,33} dt, \quad (60b)$$

$$\mathbf{v}^{33,44} = \int \hat{\mathbf{v}} \cdot \mathbf{F}^{33,44} dt, \quad (60c)$$

which add linearly to give to total recoil velocity:

$$|\mathbf{v}| = \mathbf{v}^{21,22} + \mathbf{v}^{22,33} + \mathbf{v}^{33,44}. \quad (61)$$

Note that with these definitions, the $\mathbf{v}^{\ell m, \ell' m'}$ are all real, but can be positive or negative. These different velocities are plotted in Fig. 15, with the same color scheme as in Figs. 12 and 14, along with the total recoil velocity in solid black curves. Also shown in Fig. 15 is the velocity $\mathbf{v}^{32,33}$ (dashed blue curves), defined analogously to Eq. (60a) for the $S^{32}I^{33*}$ flux terms. The small contribution from this mode pair further justifies our focus on the more dominant pairs of Eq. (21) and Fig. 4.

In the $\text{NE}_{+-}^{2:3}$ run, where the modal analysis shows the $F^{21,22}$ and $F^{33,44}$ flux terms canceling out, we see that the total recoil velocity (black curves in Fig. 15) is almost entirely dominated by the $F^{22,33}$ flux (red curves). On the other hand, for the $\text{NE}_{+-}^{2:3}$ run, the $F^{21,22}$ flux is much stronger, adding destructively with the $F^{22,33}$ flux during the RD. This has the effect of both increasing the peak velocity and also decreasing the relative strength of the antikick, due to the slow rotation frequency of the $F^{21,22}$ flux during ringdown, as described above. As expected, the $\text{NE}_{00}^{2:3}$ run displays behavior intermediate between these

two extremes. The EQ_{+-} run, however, is entirely dominated by the $F^{21,22}$ flux, and thus experiences *no* antikick, but rather drifts off slowly in a nearly constant direction, as seen in the bottom-right panel of Fig. 14.

D. Application to nonplanar kicks

One of the most remarkable results from the recent renaissance in numerical relativity was the prediction of extremely large kicks from equal-mass BHs with spins pointing opposite to each other and normal to the orbital angular momentum, producing a recoil out of the orbital plane [13–15,29]. While this configuration can produce recoils of nearly 4000 km/sec, the analogous nonprecessing configuration (the EQ_{+-} run in this paper) gives a kick of only ~ 500 km/sec in the case of maximal spin [10–12]. The multipole analysis tools developed above can be used for understanding and explaining this remarkable difference.

First, we should note that leading-order PN estimates of the linear-momentum flux during inspiral suggest that the discrepancy should be less than a factor of 2. For example, Eq. (3.31b) of Kidder [41] gives the spin-orbit contribution to the momentum flux for circular, Keplerian orbits as

$$\mathbf{F}_{\text{SO}} = \frac{16}{15} \mu^2 M \frac{\omega^2}{R^3} [\hat{\mathbf{n}} \times \Delta + (\hat{\mathbf{n}} \times \hat{\mathbf{v}})(\hat{\mathbf{v}} \cdot \Delta)], \quad (62)$$

with $\hat{\mathbf{n}}$ and $\hat{\mathbf{v}}$ being the normalized separation and velocity vectors, respectively. For spins parallel to the orbital angular momentum, the term in square brackets has magnitude Δ^z , while for planar spins, it is $2\Delta^p \sin\phi_\Delta$, where ϕ_Δ is the angle between Δ and \mathbf{n} , and Δ^p is the magnitude of Δ in the orbital plane.

Not surprisingly, we get the exact same results from the multipole analysis of Eqs. (17), (18), and (45), and one new multipole moment:

$$S_{\text{SO}}^{22} = 4i \sqrt{\frac{2\pi}{5}} \eta R \omega^3 e^{-i\phi} (\Delta^x - i\Delta^y), \quad (63)$$

while, on the other hand, the S^{21} mode is zero for the planar-spin configuration. Combining these equations, we get

$$F_x + iF_y \approx \frac{1}{336\pi} (-14iS^{21}I^{22*}) = \frac{16}{15} i \frac{\mu^2}{M} R^3 \omega^6 \Delta^z e^{i\phi}, \quad (64)$$

and using Eq. (18) we obtain

$$\begin{aligned} F_z &\approx \frac{1}{336\pi} [-28 \text{Im}(I^{22}S^{22*})] \\ &= \frac{32}{15} \frac{\mu^2}{M} R^3 \omega^6 (\Delta^x \sin\phi - \Delta^y \cos\phi) \\ &= \frac{32}{15} \frac{\mu^2}{M} R^3 \omega^6 \Delta^p \sin\phi_\Delta, \end{aligned} \quad (65)$$

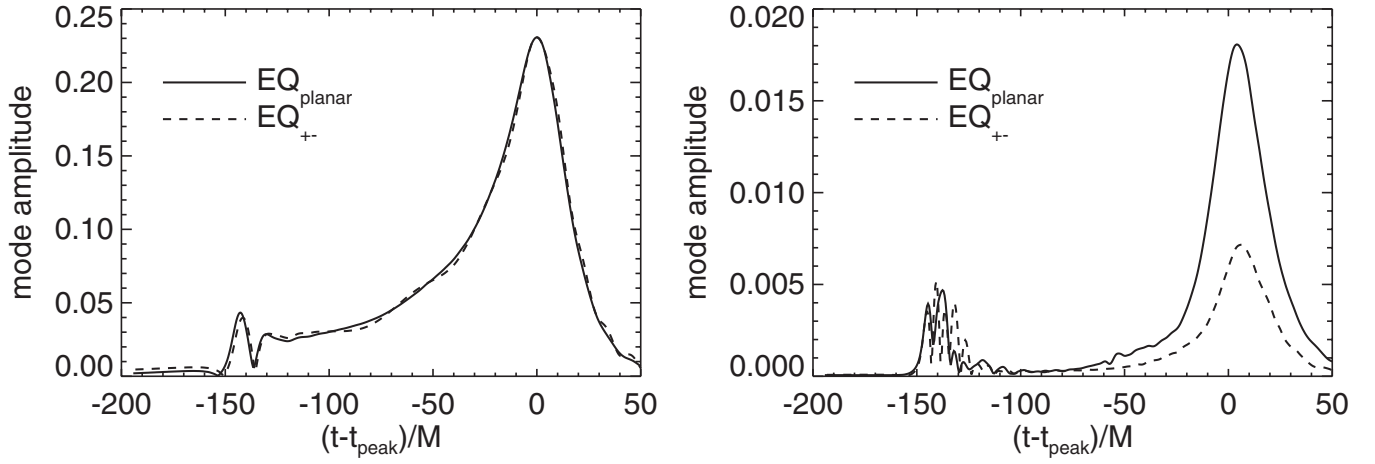


FIG. 16. Left panel: Comparison of the multipole amplitudes I^{22} for the two different equal-mass simulations: EQ_{planar} (solid line) and EQ₊₋ (dashed line). Right panel: The S^{22} amplitude from the planar-spins run (EQ_{planar}, solid line) and the S^{21} amplitude from the parallel-spins run (EQ₊₋, dashed line). We denote with t_{peak} the time at which I^{22} reaches its maximum.

where ϕ is the orbital phase of the binary. So in both paradigms, we see that, when maximizing over $\sin\phi_{\Delta}$, the planar-spin orientation should result in a recoil twice as large as the parallel-spin case, leaving a factor of roughly 4 difference unexplained.

From Eqs. (64) and (65) we see that the only relevant modes involved should be I^{22} , S^{21} , and S^{22} (for these equal-mass systems the momentum flux is dominated by a single mode pair, responsible for $\geq 95\%$ of the final recoil value). In the left panel of Fig. 16 we plot the amplitude of I^{22} from the EQ₊₋ simulation, along with that of a planar-spin simulation EQ_{planar}. All other binary parameters and the initial conditions are the same. Remarkably, the mass-quadrupole moments I^{22} are nearly identical (and domi-

nant) in both runs, and this suggests that the energy- and angular-momentum fluxes are the same [see Eqs. (31) and (32)]. This is in fact quite reasonable since the total spin of the system is zero in both cases. However, we see in the right-hand panel of Fig. 16 that the peak amplitude of the S^{22} mode is a factor of ~ 2.5 greater than that of the S^{21} mode from the EQ_{planar} and EQ₊₋ runs, respectively.

Yet Eqs. (45) and (63) suggest that these two modes should have exactly the same magnitudes, at least during the inspiral phase, and presumably during the RD as well, since the RD amplitudes are completely determined by the mode amplitudes at the matching point. It appears from Fig. 16 that S^{22} and S^{21} do in fact have the same amplitude at early times, but the relatively noisy data and short

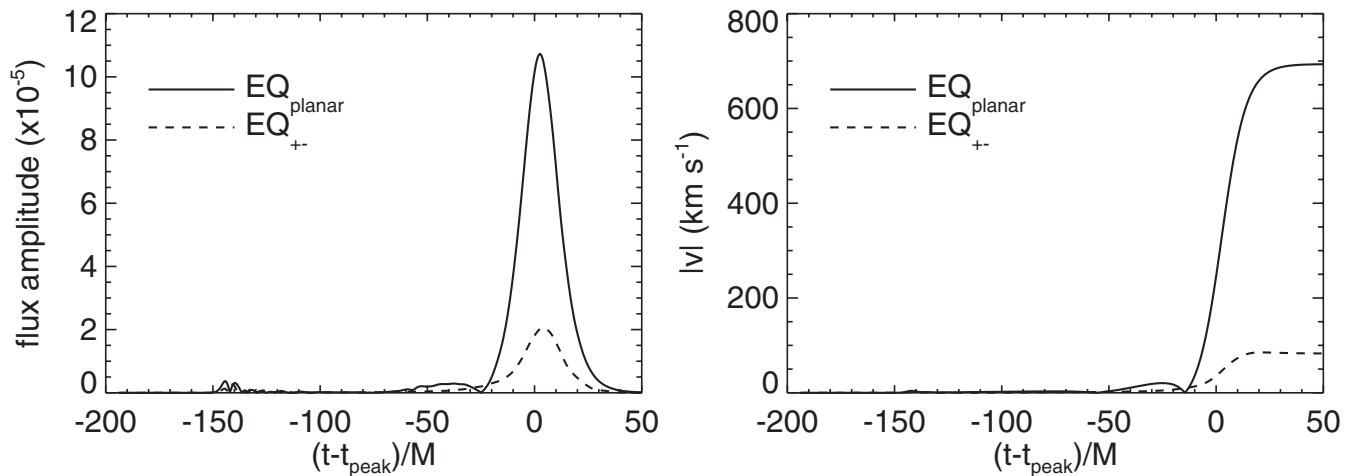


FIG. 17. Left panel: Comparison of the linear-momentum flux for the two different equal-mass simulations: EQ_{planar} (solid line) and EQ₊₋ (dashed line). Right panel: The total recoil velocity from the planar-spins run (EQ_{planar}, solid line) and the parallel-spins run (EQ₊₋, dashed line). We denote with t_{peak} the time at which I^{22} reaches its maximum.

duration of the simulations make it impossible to say for certain. If this is the case, one possible explanation for the sudden remarkable increase in the amplitude of S^{22} might be mode-coupling with the dominant I^{22} mode, as the inspiral phase begins to transition to the RD phase. This coupling is analogous to that of S^{32} and I^{22} described above in Sec. IV B, an effect that is apparently only important between modes with the same m number [72,75]. We hope to address this question in the future with longer simulations to confirm the agreement at early times, as well as other spin configurations that should enhance specific multipole modes and may help identify other similar cases of mode amplification.

Lastly, from the ringdown contribution to the velocity [Eqs. (55) and (56)], we can understand another difference between the planar- and parallel-spin orientations. Instead of having two different RD frequencies, σ_{210} and σ_{220} combine to give a slowly rotating flux vector, as in the planar-spin case, we have two *identical* RD frequencies for I^{22} and S^{22} in Eq. (65), giving precisely zero rotation to the RD flux. Furthermore, as the spin vector Δ is precessing faster and faster in a positive direction around the orbital angular-momentum vector, even during the inspiral the two modes I^{22} and S^{22} become nearly locked in phase, producing a relatively long-duration burst of linear-momentum flux in a single direction during the merger phase. Combined, these effects essentially straighten out the spiral curve in the lower right panel of Fig. 14, providing another factor of ~ 1.6 of increased recoil velocity for planar spins.

In Fig. 17 we show the combination of the above effects. In the left panel, we plot the linear-momentum flux from Eqs. (64) and (65), showing the factor of 2 increase predicted by the Kidder formula and our Eqs. (17) and (18), along with the factor of 2.5 increase in the amplitude of S^{22} relative to S^{21} . In the right panel, we plot the recoil velocity for both runs, which includes the effect of flux rotation during the merger and inspiral phases, accounting for another factor of ~ 1.6 , giving a total discrepancy of $v(\text{EQ}_{\text{planar}})/v(\text{EQ}_{+-}) \approx 2.5 \times 2 \times 1.6 = 8$.

VII. DISCUSSION

In this paper we analyzed several numerical simulations of binary BH coalescence, focusing on the physics of the recoil. We developed tools, based on the multipolar expansion [48–52], that can be used as a diagnostic of the numerical results, and understand how the recoil velocity evolves during the inspiral, merger, and ringdown phases of the coalescence.

We wrote explicit expressions for the linear-momentum flux expressed in terms of radiative multipole moments through $\ell = 4$, valid for generic spinning, precessing BH binary systems. We found that these formulas are sufficient to obtain the total recoil velocity with high accuracy. By comparing the amplitudes of the different multipole mo-

ments, we found that in the case of nonprecessing spins—and thus a recoil in the orbital plane—only three pairs of modes contribute to most of the linear-momentum flux, notably $S^{21}I^{22*}$, $I^{22}I^{33*}$, and $I^{33}I^{44*}$. Those modes account for the total recoil with an accuracy on the order of $\sim 5\%$ – 10% throughout the simulations. (See Figs. 9 and 10).

The way in which the contribution from these three pairs of modes builds up is not trivial, since not only the relative amplitudes, but especially the relative phases are also quite important. We found that the relative phases between the three mode pairs are nearly constant during the inspiral phase, but start diverging at the onset of the transition from inspiral to RD (see Fig. 13). The late-time evolution can be described reasonably well with an analytic formula obtained expressing the mode pairs in terms of fundamental QNMs of a Kerr BH. We showed that it is the relative magnitude of the current-quadrupole mode S^{21} and the mass-octupole mode I^{33} , together with the differences of the QNM fundamental frequencies for each of the dominant modes, that determine the difference between the recoil at the peak of the linear-momentum flux, and the final recoil velocity, i.e., the magnitude of the antickick.

With the final goal of improving analytic PN models, we also explored whether simple modifications of the Newtonian formula for the linear-momentum flux allow us to match the numerical results all along the binary evolution. We found that, if we treat the binary radial separation in the Newtonian multipole modes (37a)–(37e) with an effective radius, which is computed from the numerical simulations assuming that each multipole mode is described by a dominant frequency (see Fig. 2), the leading Newtonian modes reproduce quite well the numerical ones (see Figs. 7 and 8) up to the end of the inspiral phase. We also found, confirming the results in Ref. [72], that a superposition of three QNMs can fit the numerical waveforms very well from the peak of the radiation through the RD phase.

The tools developed in this paper will be employed to improve current analytic predictions for the recoil velocity [43,44] using PN analytic models [33] and the EOB approach [34–37,39,76]. An accurate, fully analytic description of the recoil velocity can be adopted in fast Monte Carlo simulations to predict recoil distributions from BH mergers with uncertainties smaller than in Ref. [47]. Those recoil distributions can in turn be included in simulations of hierarchical merger models of supermassive BHs providing more robust predictions for LISA.

ACKNOWLEDGMENTS

We thank Emanuele Berti for providing us with tabulated data for the Kerr QNM frequencies. We would like to thank the anonymous referees for their careful and constructive comments. A.B. and J.D.S. acknowledge sup-

port from NSF Grant No. PHYS-0603762, and A. B. was also supported by the Alfred P. Sloan Foundation. The work at Goddard was supported in part by NASA Grant No. 05-BEFS-05-0044 and No. 06-BEFS06-19. The simulations were carried out using Project Columbia at the NASA Advanced Supercomputing Division (Ames Research Center) and at the NASA Center for Computational Sciences (Goddard Space Flight Center). B. J. K. was supported by the NASA Postdoctoral Program at the Oak Ridge Associated Universities.

APPENDIX: RESULTS FROM 1:4 MASS RATIO

In addition to the simulations presented in the main body of this paper, we have also recently analyzed a nonspinning system with mass ratio 1:4 ($\eta = 0.16$). The results of this analysis are presented briefly in this appendix, as well as in Tables I, II, and III (labeled appropriately as $\text{NE}_{00}^{1:4}$). More details can be found in Ref. [76].

In Fig. 18 we show the flux amplitudes from the different modes, as in Fig. 4 above. We find the relative amplitudes almost identical to those of the $\text{NE}_{00}^{1:2}$ run, with a slightly stronger contribution from the I^{44} mode, as expected from Eq. (37g), which predicts a maximum in the I^{44} amplitude for $\eta = 0.167$.

In Fig. 19 we plot the phase relations between the different flux vectors, defined in Eqs. (49a)–(49c). As anticipated in Sec. VIB above, we find a smaller phase shift in ψ^{3-4} at the transition from inspiral to ringdown for this more extreme mass-ratio system. The other phases appear to behave as expected.

Lastly, in Fig. 20, we show the total recoil velocity along with the relative contributions from the dominant modes for the $\text{NE}_{00}^{1:4}$ run. Again, the qualitative behavior is quite similar to the $\text{NE}_{00}^{2:3}$ and $\text{NE}_{00}^{1:2}$ runs, but we can now

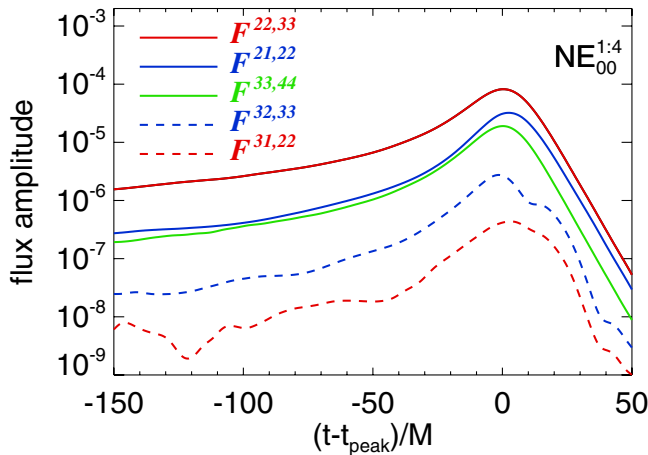


FIG. 18 (color online). Flux amplitudes from the $\text{NE}_{00}^{1:4}$ run, as in Fig. 4.

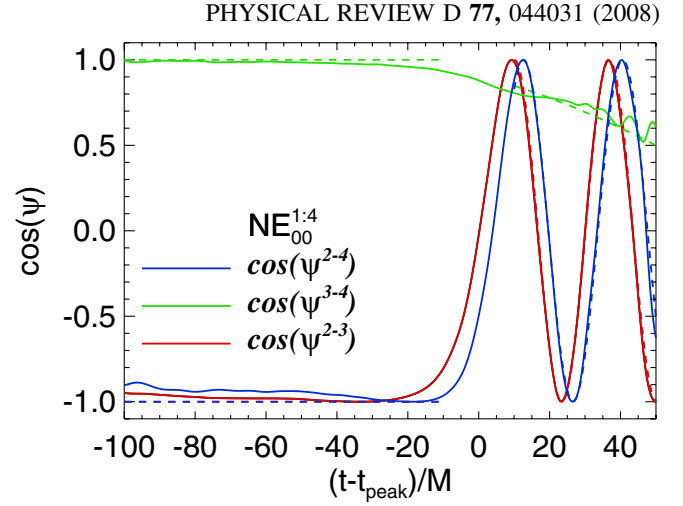


FIG. 19 (color online). Phase differences from the $\text{NE}_{00}^{1:4}$ run, as in Fig. 13.

identify a clear trend of a smaller antikick for smaller values of η . As mentioned above in Sec. VIC, the amplitude of the antikick is most strongly dependent on the relative amplitudes of the S^{21} and I^{33} modes, but for nonspinning BH binaries, these modes both scale the same with the mass ratio. However, the amplitude of the I^{22} mode decreases with decreasing η , while the amplitude of I^{44} increases with decreasing η , at least over the range considered here. Thus the amplitude of the $F^{33,44}$ flux increases relative to the $F^{22,33}$ flux for more extreme mass ratios. From Figs. 15 and 20, we see that the $F^{22,33}$ flux dominates the antikick, while the $F^{33,44}$ flux contributes almost nothing to it, so by increasing the relative amplitude of $F^{33,44}$, we have effectively decreased the size of the antikick.

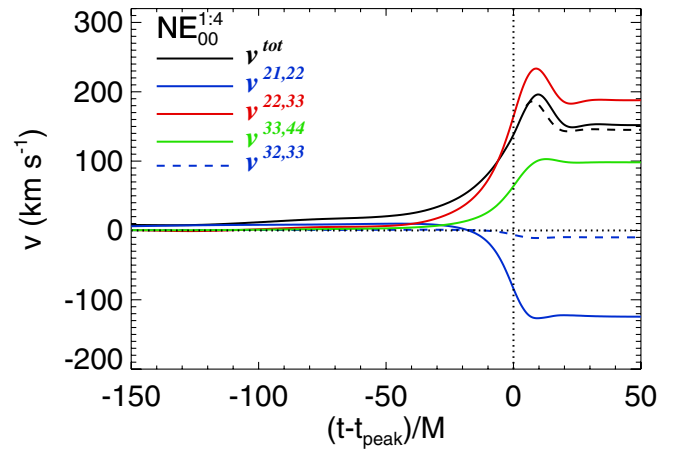


FIG. 20 (color online). Relative contributions to the total recoil velocity from the different multipole mode pairs for the $\text{NE}_{00}^{1:4}$ run, as in Fig. 15.

- [1] F. Pretorius, Phys. Rev. Lett. **95**, 121101 (2005).
- [2] M. Campanelli, C.O. Lousto, P. Marronetti, and Y. Zlochower, Phys. Rev. Lett. **96**, 111101 (2006).
- [3] J. Baker, J. Centrella, D. Choi, M. Koppitz, and J. van Meter, Phys. Rev. Lett. **96**, 111102 (2006).
- [4] U. Sperhake, Phys. Rev. D **76**, 104015 (2007).
- [5] J. González, U. Sperhake, B. Brügmann, M. Hannam, and S. Husa, Phys. Rev. Lett. **98**, 091101 (2007).
- [6] B. Szilagyi, D. Pollney, L. Rezzolla, J. Thornburg, and J. Winicour, Classical Quantum Gravity **24**, S275 (2007).
- [7] F. Herrmann, I. Hinder, D. Shoemaker, and P. Laguna, Classical Quantum Gravity **24**, S33 (2007).
- [8] J.G. Baker, J. Centrella, D. Choi, M. Koppitz, J.R. van Meter, and M.C. Miller, Astrophys. J. **653**, L93 (2006).
- [9] J.A. Gonzalez, U. Sperhake, B. Brügmann, M. Hannam, and S. Husa, Phys. Rev. Lett. **98**, 091101 (2007).
- [10] F. Herrmann, I. Hinder, D. Shoemaker, P. Laguna, and R.A. Matzner, Astrophys. J. **661**, 430 (2007).
- [11] M. Koppitz, D. Pollney, C. Reisswig, L. Rezzolla, J. Thornburg, P. Diener, and E. Schnetter, Phys. Rev. Lett. **99**, 041102 (2007).
- [12] J.G. Baker, W.D. Boggs, J. Centrella, B.J. Kelly, S.T. McWilliams, M.C. Miller, and J.R. van Meter, Astrophys. J. **668**, 1140 (2007).
- [13] J.A. Gonzalez, M.D. Hannam, U. Sperhake, B. Brügmann, and S. Husa, Phys. Rev. Lett. **98**, 231101 (2007).
- [14] W. Tichy and P. Marronetti, Phys. Rev. D **76**, 061502 (2007).
- [15] M. Campanelli, C.O. Lousto, Y. Zlochower, and D. Merritt, Astrophys. J. **659**, L5 (2007).
- [16] W.B. Bonnor and M.A. Rotenberg, Proc. R. Soc. A **265**, 109 (1961).
- [17] A. Peres, Phys. Rev. **128**, 2471 (1962).
- [18] J.D. Bekenstein, Astrophys. J. **183**, 657 (1973).
- [19] F.I. Cooperstock, Astrophys. J. **213**, 250 (1977).
- [20] M.J. Fitchett, Mon. Not. R. Astron. Soc. **203**, 1049 (1983); M.J. Fitchett and S. Detweiler, Mon. Not. R. Astron. Soc. **211**, 933 (1984).
- [21] M.G. Haehnelt, Mon. Not. R. Astron. Soc. **269**, 199 (1994); K. Menou, Z. Haiman, and V.K. Narayanan, Astrophys. J. **558**, 535 (2001); M. Volonteri, F. Haardt, and P. Madau, Astrophys. J. **582**, 559 (2003).
- [22] D. Merritt, M. Milosavljevic, M. Favata, and S.A. Hughes, Astrophys. J. **607**, L9 (2004).
- [23] M. Volonteri, Astrophys. J. **663**, L5 (2007).
- [24] J.D. Schnittman, Astrophys. J. **667**, L133 (2007).
- [25] M.G. Haehnelt, M.B. Davies, and M.J. Rees, Mon. Not. R. Astron. Soc. **366**, L22 (2006).
- [26] E.W. Bonning and G.A. Shields, Astrophys. J. **666**, L13 (2007).
- [27] M. Boylan-Kolchin, C.-P. Ma, and E. Quataert, Astrophys. J. **613**, L37 (2004).
- [28] T.R. Lauer *et al.*, Astrophys. J. **662**, 808 (2007).
- [29] B. Brügmann, J.A. Gonzalez, M. Hannam, S. Husa, and U. Sperhake, arXiv:0707.0135.
- [30] J.D. Schnittman, Phys. Rev. D **70**, 124020 (2004).
- [31] T. Bogdanovic, C.S. Reynolds, and M.C. Miller, Astrophys. J. **661**, L147 (2007).
- [32] A. Loeb, Phys. Rev. Lett. **99**, 041103 (2007).
- [33] See, e.g., L. Blanchet, Living Rev. Relativity **5**, 3 (2002).
- [34] T. Damour, B. R. Iyer, and B. S. Sathyaprakash, Phys. Rev. D **57**, 885 (1998).
- [35] A. Buonanno and T. Damour, Phys. Rev. D **59**, 084006 (1999).
- [36] A. Buonanno and T. Damour, Phys. Rev. D **62**, 064015 (2000).
- [37] T. Damour, P. Jaranowski, and G. Schäfer, Phys. Rev. D **62**, 084011 (2000).
- [38] T. Damour, P. Jaranowski, and G. Schäfer, Phys. Rev. D **62**, 044024 (2000).
- [39] A. Buonanno, Y. Chen, and T. Damour, Phys. Rev. D **74**, 104005 (2006).
- [40] A. Wiseman, Phys. Rev. D **46**, 1517 (1992).
- [41] L. Kidder, Phys. Rev. D **52**, 821 (1995).
- [42] M. Favata *et al.*, Astrophys. J. **607**, L5 (2004).
- [43] L. Blanchet, M. S. S. Qusailah, and C. M. Will, Astrophys. J. **635**, 508 (2005).
- [44] T. Damour and A. Gopakumar, Phys. Rev. D **73**, 124006 (2006).
- [45] C.F. Sopuerta, N. Yunes, and P. Laguna, Astrophys. J. **656**, L9 (2007).
- [46] R. H. Price and J. Pullin, Phys. Rev. Lett. **72**, 3297 (1994).
- [47] J.D. Schnittman and A. Buonanno, Astrophys. J. **662**, L63 (2007).
- [48] K. S. Thorne, Rev. Mod. Phys. **52**, 299 (1980).
- [49] L. Blanchet and T. Damour, Ann. Inst. Henri Poincaré **50**, 377 (1989).
- [50] L. Blanchet and G. Schäfer, Mon. Not. R. Astron. Soc. **239**, 845 (1989).
- [51] L. Blanchet, T. Damour, and G. Schäfer, Mon. Not. R. Astron. Soc. **242**, 289 (1990).
- [52] W. Junker and G. Schäfer, Mon. Not. R. Astron. Soc. **254**, 146 (1992).
- [53] C. V. Vishveshwara, Nature (London) **227**, 936 (1970); M. Davis, R. Ruffini, W. H. Press, and R. H. Price, Phys. Rev. Lett. **27**, 1466 (1971); W. Press, Astrophys. J. **170**, L105 (1971); M. Davis, R. Ruffini, and J. Tiomno, Phys. Rev. D **5**, 2932 (1972); S. Chandrasekhar and S. Detweiler, Proc. R. Soc. A **344**, 441 (1975).
- [54] C. W. Misner, K. S. Thorne, and J. A. Wheeler, *Gravitation* (W.H. Freeman, San Francisco, 1973).
- [55] J. Baker, M. Campanelli, and C. Lousto, Phys. Rev. D **65**, 044001 (2002).
- [56] J.G. Baker, S.T. McWilliams, J.R. van Meter, J. Centrella, D.I. Choi, B.J. Kelly, and M. Koppitz, Phys. Rev. D **75**, 124024 (2007).
- [57] J.N. Goldberg, A.J. Macfarlane, E.T. Newman, F. Rohrlich, and E.C.G. Sundarshan, J. Math. Phys. (N.Y.) **8**, 2155 (1967).
- [58] Y. Wiaux, L. Jacques, and P. Vanderghenst, J. Comput. Phys. **226**, 2359 (2007).
- [59] S. Brandt and B. Brügmann, Phys. Rev. Lett. **78**, 3606 (1997).
- [60] J.D. Brown and L.L. Lowe, J. Comput. Phys. **209**, 582 (2005).
- [61] J. Bowen and J.W. York, Phys. Rev. D **21**, 2047 (1980).
- [62] D. Christodoulou, Phys. Rev. Lett. **25**, 1596 (1970); D. Christodoulou and R. Ruffini, Phys. Rev. D **4**, 3552 (1971).
- [63] B. Imbiriba, J.G. Baker, D.-I. Choi, J. Centrella, D.R. Fiske, J.D. Brown, J.R. van Meter, and K. Olson, Phys.

- Rev. D **70**, 124025 (2004).
- [64] M. Shibata and T. Nakamura, Phys. Rev. D **52**, 5428 (1995); T. W. Baumgarte and S. L. Shapiro, Phys. Rev. D **59**, 024007 (1998).
 - [65] P. Hübner, Classical Quantum Gravity **16**, 2823 (1999).
 - [66] M. D. Duez, S. L. Shapiro, and H.-J. Yo, Phys. Rev. D **69**, 104016 (2004).
 - [67] J. van Meter, J. G. Baker, M. Koppitz, and D.-I. Choi, Phys. Rev. D **73**, 124011 (2006).
 - [68] J. G. Baker and J. van Meter, Phys. Rev. D **72**, 104010 (2005).
 - [69] P. MacNeice, K. Olson, C. Mobarrry, R. de Fainchtein, and C. Packer, Comput. Phys. Commun. **126**, 330 (2000).
 - [70] K. Martel and E. Poisson, Phys. Rev. D **71**, 104003 (2005).
 - [71] E. Berti *et al.*, Phys. Rev. D **76**, 064034 (2007).
 - [72] A. Buonanno, G. Cook, and F. Pretorius, Phys. Rev. D **75**, 124018 (2007).
 - [73] E. W. Leaver, Proc. R. Soc. A **402**, 285 (1985).
 - [74] F. Echeverria, Phys. Rev. D **40**, 3194 (1989).
 - [75] E. Berti, V. Cardoso, and C. Will, Phys. Rev. D **73**, 064030 (2006).
 - [76] A. Buonanno, Y. Pan, J. G. Baker, J. Centrella, B. J. Kelly, S. T. McWilliams, and J. R. van Meter, Phys. Rev. D **76**, 104049 (2007).
 - [77] L. Blanchet and B. Iyer, Classical Quantum Gravity **20**, 755 (2003).
 - [78] L. Blanchet, A. Buonanno, and G. Faye, Phys. Rev. D **74**, 104034 (2006); **75**, 049903(E) (2007).